Pacific Northwest
NATIONAL LABORATORY

PNNL-38868

Advanced Methods for High Energy Radiography

Multi-energy Radiography for Materials Discrimination Feasibility Report

December 2025

Andrew J. Gilbert
Luke W. Campbell
Dustin M. Kasparek
Paul B. Rose, Oak Ridge National Laboratory
Erin A. Miller

U.S. DEPARTMENT OF ENERGY

Prepared for the U.S. Department of Energy
under Contract DE-AC05-76RL01830

DISCLAIMER

This report was prepared as an account of work sponsored by an agency of the United States Government. Neither the United States Government nor any agency thereof, nor Battelle Memorial Institute, nor any of their employees, makes **any warranty, express or implied, or assumes any legal liability or responsibility for the accuracy, completeness, or usefulness of any information, apparatus, product, or process disclosed, or represents that its use would not infringe privately owned rights**. Reference herein to any specific commercial product, process, or service by trade name, trademark, manufacturer, or otherwise does not necessarily constitute or imply its endorsement, recommendation, or favoring by the United States Government or any agency thereof, or Battelle Memorial Institute. The views and opinions of authors expressed herein do not necessarily state or reflect those of the United States Government or any agency thereof.

PACIFIC NORTHWEST NATIONAL LABORATORY
operated by
BATTELLE
for the
UNITED STATES DEPARTMENT OF ENERGY
under Contract DE-AC05-76RL01830

Printed in the United States of America

Available to DOE and DOE contractors from
the Office of Scientific and Technical Information,
P.O. Box 62, Oak Ridge, TN 37831-0062
www.osti.gov
ph: (865) 576-8401
fax: (865) 576-5728
email: reports@osti.gov

Available to the public from the National Technical Information Service
5301 Shawnee Rd., Alexandria, VA 22312
ph: (800) 553-NTIS (6847)
or (703) 605-6000
email: info@ntis.gov
Online ordering: http://www.ntis.gov

PNNL-38868

Advanced Methods for High Energy Radiography

Multi-energy Radiography for Materials Discrimination Feasibility Report

December 2025

Andrew J. Gilbert
Luke W. Campbell
Dustin M. Kasparek
Paul B. Rose, Oak Ridge National Laboratory
Erin A. Miller

Prepared for
the U.S. Department of Energy
under Contract DE-AC05-76RL01830

Pacific Northwest National Laboratory
Richland, Washington 99354

Abstract

This report details a study of information contained in high-energy (MeV), dual-energy radiography data for the purpose of materials discrimination, using computational methods and analysis of real radiography data. We use a computational method, the Cramer-Rao lower bound (CRLB) to measure information content in a dual-energy radiograph and bound uncertainties on material discrimination for a wide range of radiography system and object geometry realizations. We conduct computational studies of an inverse algorithm to determine material composition using simulated data. and assess the impact of systematic effects such as scattered radiation. Finally, we apply the methods to experimental data, benchmarking the CRLB to material discrimination analysis of high-energy, dual-energy radiography data and exploring a method to make an effective dual-energy scan with a single X-ray shot by using a patterned grid in the X-ray image. We find that although material discrimination is fundamentally limited, broad discrimination between high and low atomic number materials is possible. The Cramer-Rao lower bound on uncertainty tracks well with more complex approaches and with measured data, and may provide a useful tool for system design and optimization. Finally, the use of a patterned optic may enable single shot dual energy imaging when acquiring two shots is not feasible.

Executive summary

This report details a study of information contained in high-energy (MeV), dual-energy radiography data for the purpose of materials discrimination, using computational methods and analysis of real radiography data.

In Section 2.0, we introduce a method, the Cramer Rao lower bound (CRLB), to compute the minimum uncertainty expected from determining a material thickness from a given set of radiography data with random variations due to counting statistics. An example of this is shown in Figure 1. The study confirmed that material discrimination at MeV energies is difficult, largely driven by the fact that the X-ray attenuation coefficients for a wide range of material Z show similar energy-dependent profiles largely due to Compton scatter effects that dominate the X-ray interactions from ~500 keV to ~ 4 MeV. This limits the information that is available for discrimination. Nonetheless, discrimination between broad categories of high-Z and low-Z materials appears feasible. Further studies showed that using high-Z materials as beam filters is optimal and that lower endpoint energy spectra may not improve material discrimination if the beam flux is lower at those energies, which is typical for X-ray betatron sources.

In Section 3.0, we use physical models and introduce an inverse algorithm to determine material thicknesses from the dual-energy radiography data. This allows comparison of uncertainties observed from the output of an inverse algorithm, a least-squares misfit, and how it compares to the uncertainties calculated from the CRLB. We found good agreement between trends of the algorithm output compared to the CRLB calculations. Furthermore, we explored the effect of systematic uncertainties in the physics model used in the inverse algorithm, which the CRLB cannot capture. It was found that inaccurate scatter models affect material discrimination considerably. However, if the scatter is known to good accuracy and used in the inverse algorithm, the systematic errors are corrected, and nominal material discrimination is recovered.

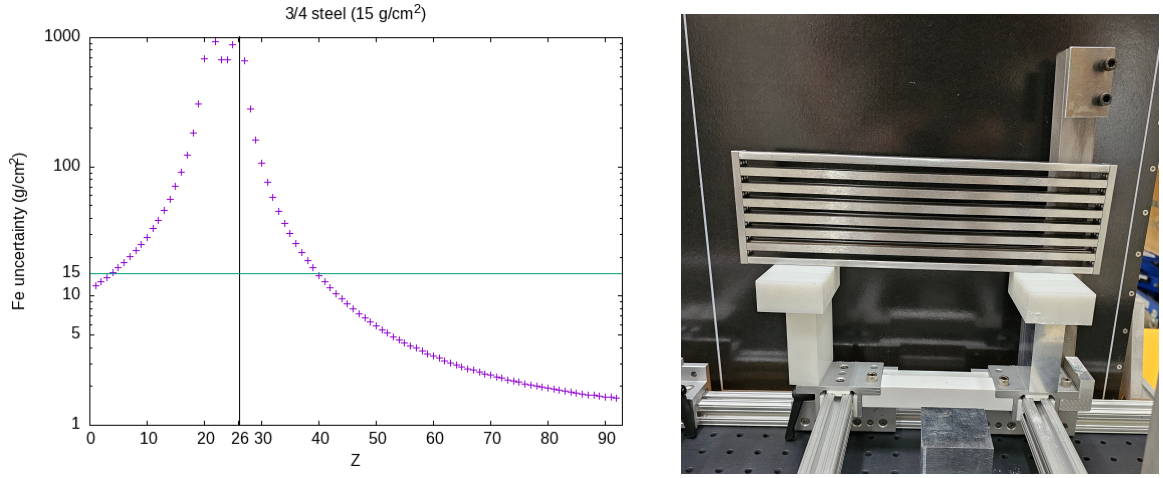


Figure 1. (left) The CRLB on uncertainty for discriminating iron from any other element in the periodic table (listed by atomic number Z in the x-axis), for a 3/4" thick steel slab. The position of Z=26 for iron is marked with a vertical black line. Lower uncertainty indicates better material discrimination. (right) A picture of the patterned grid placed in front of the image plane to be used to generate lower-energy (unfiltered) and higher-energy (filtered) data in a single X-ray image.

In Section 4.0, the theoretical work in the previous sections was tested with real high-energy, dual-energy X-ray radiography. We find that the CRLB calculations compare well to material discrimination observed with real data and the inverse algorithm. The ability to complete accurate material estimation requires accurate physical models, and the work was somewhat limited here by the presence of scatter in the radiography data. Furthermore, this section detailed the feasibility of completing dual-energy radiography with a single shot through the use of a coarse grid that produces interspersed attenuated and unattenuated regions in the image, as shown in Figure 1. Though this does reduce the effective spatial resolution of the system, preliminary results indicate that material discrimination between low- and high-Z materials is feasible in this regime. This is an important conclusion that indicates methods like this could be used for material discrimination when time or space limitations prevent a full dual-energy scan to be made.

In summary, the ability to complete material discrimination with high-energy X-ray radiography is limited, largely by the limited material information that is encoded in the transmitted X-ray beam. Nonetheless, the system can be designed to optimize the amount of material information that is available. Results from this report lead to the following recommendations for future research:

1. Targeted imaging system design with the Cramer-Rao lower bound (CRLB). The work presented here shows that uncertainties from the CRLB track well with uncertainties from an inverse algorithm and real X-ray data. This suggests that the CRLB calculations could be used to determine what level of information can be determined from the radiography data, and how to design the system better to increase the information available from the data. For example, calculations like this would help to frame developments in X-ray sources and detectors that would be particularly beneficial for a given task. As monoenergetic sources are designed, higher-efficiency detector materials are developed, and high-energy spectral imaging becomes feasible, bringing methods like this alongside the equipment development would inform which capabilities of future high-energy radiography systems will be particularly beneficial for material discrimination.

2. Development of fast, accurate physics (forward) models for high-energy radiography systems. Computational studies in this report show the importance of having an accurate physics model for any quantitative image analysis. High-energy radiography systems used in this report could be better understood. In particular, the report found that knowing the X-ray spectrum and reducing or estimating the scatter component is particularly important. Low-energy X-ray radiography systems in the 100s-of-keV range are well understood given their ubiquitous use in the medical and security fields. While high-energy radiography systems can be niche in their uses, their range of use is increasing, particularly for cargo inspection and nondestructive evaluation.

3. Imaging system design for completing single-shot, dual-energy radiography using a coarse grating. Experiments presented here were preliminary and explored a limited range of material geometries and compositions. However, the results suggest that more can be done to enable single-shot dual-energy radiography. Further exploration of grid design, including the trade-offs between grid period and available information, would make the method fieldable. The single-shot method would be useful if time or space constraints limit the ability to complete a typical dual-energy X-ray shot.

Acknowledgments

This work was supported by the Office of Defense Nuclear Nonproliferation Research and Development within the U.S. Department of Energy's National Nuclear Security Administration.

Contents

Abstract ii
Executive summary iii
Acknowledgments v
1.0 Introduction 1
2.0 Statistical limits on uncertainty in dual-energy radiography 2
2.1 Introduction 2
2.2 Setting 3
2.3 Variance 3
2.4 Spectrum and Response Function 5
2.5 Constructing the information matrix 7
2.6 Calculation Set 1: Basic Material Discrimination 8
2.6.1 Results 9
2.6.2 Discussion 9
2.7 Calculation Set 2: Effects of Filtration and Choice of Filters 10
2.7.1 Discussion 13
2.8 Calculation Set 3: Spectra With Different Endpoint Energies 14
2.8.1 Spectra 14
2.8.2 Procedure 15
2.8.3 Results 15
2.8.4 Discussion 22
2.9 Calculation set 4: Material Discrimination Over the Entire Periodic Table 22
2.9.1 Procedure 22
2.9.2 Results 22
2.9.3 Discussion 23
2.10 Overall Discussion and Conclusions 24
3.0 Inverse modeling to study material discrimination in dual-energy radiography 26
3.1 A simple test of the Cramer Rao lower bound 27
3.2 A computational study on the effect of scatter 28
4.0 Experimental material discrimination 32
4.1 Experimental data acquisition 32
4.2 Material discrimination using filtered spectra for dual energy radiography 33
4.3 Material discrimination using a single-shot dual-energy grid 36
5.0 Conclusions and future work 41
6.0 References 43
Appendix A – Cramer Rao lower bound calculation raw results A.1

Figures

Figure 1. (left) The CRLB on uncertainty for discriminating iron from any other element in the periodic table (listed by atomic number Z in the x-axis), for a 3/4" thick steel slab. The position of Z=26 for iron is marked with a vertical black line. Lower uncertainty indicates better material discrimination. (right) A picture of the patterned grid placed in front of the image plane to be used to generate lower-energy (unfiltered) and higher-energy (filtered) data in a single X-ray image. iii

Figure 2. A representative exposure of the set of exposures used to measure the variance. 4

Figure 3. Mean and variance of pixel values from all good pixels of the exposure sequence (purple crosses) with the fit function shown as a green line. 5

Figure 4. Betatron X-ray spectra normalized to unit weight with 7.5 MeV endpoint energy, with and without filtering. 6

Figure 5. Efficiency of the detector. 7

Figure 6. The mass attenuation coefficients of the four materials used 8

Figure 7. The mass attenuation coefficients of the four materials used, superimposed on the two spectra. 10

Figure 8. Cramér-Rao lower bound uncertainty distinguishing between tungsten and aluminum, with known 12.2 g/cm^2 tungsten sample, as a function of filter thickness and composition. 11

Figure 9. Cramér-Rao lower bound uncertainty distinguishing between tungsten and aluminum as a function of the thickness of a tungsten filter, for different thicknesses of tungsten objects. 12

Figure 10. Cramér-Rao lower bound uncertainty distinguishing between tungsten and aluminum as a function of the thickness of filters of different materials, for different targets used in the experimental campaign. 13

Figure 11. Normalized photon spectra grouped by endpoint energy with different tungsten filter thickness. 15

Figure 12. Uncertainly of aluminum (top) and tungsten (bottom) measurements of a 1 inch aluminum slab, for dual-energy measurements using the 4 MV/4 MV (open orange squares), 4 MV/7.5 MV (filled yellow squares), or 7.5 MV/7.5 MV (open orange squares) spectral pairs. The filter thickness is the thickness of tungsten for the second listed spectrum; the first spectrum is always filtered with 1 mm tungsten. 16

Figure 13. Uncertainly of aluminum (top) and tungsten (bottom) measurements of a 2 inch aluminum slab, for dual-energy measurements using the 4 MV/4 MV (open orange squares), 4 MV/7.5 MV (filled yellow squares), or 7.5 MV/7.5 MV (open orange squares) spectral pairs. The filter thickness is the thickness of tungsten for the second listed spectrum; the first spectrum is always filtered with 1 mm tungsten. 17

Figure 14. Uncertainly of aluminum (top) and tungsten (bottom) measurements of a ¼ inch tungsten slab, for dual-energy measurements using combinations of the 4 MV and 7.5 MV beams. The 4 MV source is scaled to give 1/10th the signal of the 7.5 MV source. The filter thickness is the thickness of

tungsten for the second listed spectrum; the first spectrum is always filtered with 1 mm tungsten. 18

Figure 15. Uncertainly of aluminum (top) and tungsten (bottom) measurements of a 1 inch aluminum slab, for dual-energy measurements using combinations of the 4 MV and 7.5 MV beams, when the 4 MV spectrum gives the same signal as the 7.5 MV spectrum. The filter thickness is the thickness of tungsten for the second listed spectrum; the first spectrum is always filtered with 1 mm tungsten. 19

Figure 16. Uncertainly of aluminum (top) and tungsten (bottom) measurements of a 2 inch aluminum slab, for dual-energy measurements using combinations of the 4 MV and 7.5 MV beams, when the 4 MV spectrum gives the same signal as the 7.5 MV spectrum. The filter thickness is the thickness of tungsten for the second listed spectrum; the first spectrum is always filtered with 1 mm tungsten. 20

Figure 17. Uncertainly of aluminum (top) and tungsten (bottom) measurements of a ¼ inch tungsten slab, for dual-energy measurements using combinations of the 4 MV and 7.5 MV beams, when the 4 MV spectrum gives the same signal as the 7.5 MV spectrum. The filter thickness is the thickness of tungsten for the second listed spectrum; the first spectrum is always filtered with 1 mm tungsten. 21

Figure 18. The lower bound to uncertainty for discriminating iron from any other element in the periodic table (listed by atomic number Z in the x-axis), for two steel slabs (assumed pure iron for this exercise) of different thicknesses. The position of Z=26 for iron is marked with a vertical black line. The actual thicknesses of the slabs are marked with a horizontal green line. 23

Figure 19. (left) A simple, simulated radiograph of material slabs. (right) Material estimation output for a two-material set of poly and tungsten (W). 27

Figure 20. Line profiles of the material thicknesses estimated for the spectra: (a) [7.5 MV, 7.5 filtered], (b) [4 MV, 7.5 MV filtered], and (c) [4 MV, 7.5 MV]. Actual thicknesses are shown for each material as a lighter shade, to compare to those values estimates. 28

Figure 21. Line profiles of the material thicknesses estimated from the inverse algorithm when different levels of scatter are present in the image data, compared to the actual, for a range of scatter levels. The added scatter is a flat profile, percentage of the background, unattenuated regions of the simulated image data. 30

Figure 22. Line profiles of material estimates from the inverse algorithm when a significant portion of the modeled image data is scatter, 50%. (a) Estimates when the inverse algorithm does not include a model of the scatter. (b) Estimates when the inverse algorithm has an accurate scatter model. 31

Figure 23. (left) The JME betatron used for the material discrimination experiments. (right) The imaging system, showing the poly material blocks in the foreground and the imaging detector in the background. 32

Figure 24. Steel slabs material estimations between steel and tungsten basis functions. Discrimination appears good, though accuracy is limited by the large scatter contribution shown in Figure 25. (left) Shows the materials

estimated at each image pixel and (right) shows a line profile through the middle of the result images. 33
Figure 25. (left) Image data of the steel slabs object using high-energy spectrum with 3/4” thick tungsten for beam filtration. (right) The horizontal line profile of the data. Blurred material edges is a clear indication of a large scatter environment..... 34
Figure 26. An example of material estimation algorithm results for a difficult material discrimination problem, here discriminating between basis functions of steel and poly. 34
Figure 27. A measure of materials discrimination (separation) is given for all of the slabs data. Higher values indicate that there is greater separation between the estimated slab material and that of the second basis material, scanned for all elements of the periodic table. Higher values are better and the dotted line indicates the location of the slab material on the x-axis. 35
Figure 28. (left) A picture of the coarse grid placed in front of the image plane and (right) a drawing of the grid. This is a patterning element to be used to generate lower-energy (unfiltered) and higher-energy (filtered) data in a single image..... 36
Figure 29. (top) The original image data with the coarse grid in place in the center of the image. This image also has two thicknesses of aluminum in front of the coarse grid. (middle) The processed unfiltered image data and (bottom) the processed filtered image data. 37
Figure 30. (left) A region of interest from the coarse grid data. (right) A line profile, shown in the left, from the grid data..... 38
Figure 31. Low energy attenuation and high-energy attenuation calculated from regions of interest from the processed coarse grid data, e.g., Figure 29, for each material. The slope of the lines can be used for material identification..... 39

Tables

Table 1. Slab composition and thickness..... 3
Table 2. Numerical uncertainties estimated from the Cramer Rao lower bound (CRLB) framework introduced in Section 2.0. 28
Table 3. Summary of material slopes shown in Figure 30. 39

1.0 Introduction

X-ray imaging is a powerful tool for noninvasively inspecting the internal structure of objects and is widely used across the medical, security, and nondestructive evaluation fields. Dual-energy X-ray imaging allows material discrimination based on physical properties, such as a material's density and atomic number. Dual-energy radiography is widely used in medical and security fields [Fainberg, 1992]. In general, dual-energy radiography is limited in its ability to distinguish materials with similar attenuation coefficients or materials that are part of a mixture or composite [Azevedo, 2016] [Tobias, 2019]. In part, this is because these techniques only pick up on broad differences in material attenuation properties averaged over wide ranges of energy.

High-energy radiography is being used for inspection of cargo for discovery of drugs, explosives, and special nuclear material [Runkle, 2009]. Compared to lower-energy X-ray radiography for medical and security applications, cargo radiography requires higher-energy X-rays in order to see through the large container. Cargo scanning systems use linear accelerator produced X-rays with energies up to 9 MeV [Ogorodnikov, 2002]. Early material discrimination studies used dual-energy radiography data to determine an average atomic number Z and density through a given X-ray path length. These studies showed the ability to discriminate between low-, and high-atomic-numbered materials in a single-layer configuration with the aid of image processing algorithms to reduce noise in the processed images.

Compared to lower-energy radiography systems, research into the capabilities and limitations of high-energy (MeV), dual-energy radiography systems is rather limited. In this report, we seek to fill some of that gap. We build on our experience with betatron-based high-energy radiography to look into the fundamental information content from these dual-energy systems for the purpose of materials discrimination. We start by presenting a computational method, the Cramer-Rao lower bound (CRLB) to measure information content in a dual-energy radiograph using methods developed for low-energy radiography [Roessl, 2009]. The CRLB allows quick computations to assess information content, in uncertainties on material discrimination, for a wide range of radiography system and object geometry realizations. Next, we complete computational studies of the uncertainties observed by using an inverse algorithm to determine material composition using straightforward, simulated data. This connects the uncertainty calculations with the numerical results from the inverse algorithm, here a least-squares fit with a physics model of the radiography system. Finally, we apply the methods to experimental data, benchmarking the CRLB to material discrimination analysis of high-energy, dual-energy radiography data. Here, we also detail a method to make an effective dual-energy scan with a single X-ray shot by using a patterned grid in the X-ray image.

2.0 Statistical limits on uncertainty in dual-energy radiography

2.1 Introduction

We begin the study on the feasibility of materials discrimination with high-energy, dual-energy radiography with a computational study. Information theory can help us study a wide range of possible material geometries and X-ray spectra, though it is limited by the accuracy of the physical models that underpin the computational study. Previous work has shown that computation studies can be a useful tool for framing out experiment design [Gilbert, 2025], and here we extend the previous work to a measure of absolute information content, rather than a relative measure as was used previously. Absolute measures of uncertainties allow us to understand the uncertainties quantitatively that will result from common inverse problem methods, such as least squares misfit, better limiting what we can expect to be possible, or not, for materials discrimination with high-energy dual-energy X-ray radiography.

Here, the computational studies are constrained by spectra, objects, and detectors that we have available to produce experimental data. This will allow us to benchmark the computational studies to experimental data so that we can be confident in applying the computations to a wider range of scenarios.

Any real measurement contains a finite amount of information that can be picked out from the background noise. This can be quantified as the Fischer information of an observation. Roessl and Herrmann [Roessl, 2009] show that for a series of energy-integrating radiographs with different spectra on the same object, the Fischer information matrix takes the form

$$\mathcal{F}_{\alpha\beta} = \sum_{i=1}^{N} \frac{1}{\sigma_i^2} \frac{\partial I_i}{\partial \lambda_\alpha} \frac{\partial I_i}{\partial \lambda_\beta} + \frac{1}{2} \sum_{i=1}^{N} \frac{1}{\left(\sigma_i^2\right)^2} \frac{\partial \sigma_i^2}{\partial \lambda_\alpha} \frac{\partial \sigma_i^2}{\partial \lambda_\beta}. \quad (1)$$

for derived values λ_α and λ_β given N measurements of a quantity I_i, $1 \leq i \leq N$ with measurement variance σ_i^2. In our problem, I_i is the intensity measured behind an object for spectrum i, and λ_α is the areal density of material α that the X-rays passed through on their way to the detector.

Once $\mathcal{F}$ is found, the lower bound for the variance of the derived values is given by

$$C_{\alpha\alpha} \geq \mathcal{F}_{\alpha\alpha}^{-1}$$

where $C_{\alpha\beta}$ is the covariance matrix. This inequality gives us the Cramér-Rao lower bound for the variance of estimates of the material areal densities. Note that this method does not give any method for distinguishing what the areal densities actually are, only that if a method is available we can put a lower limit on the uncertainty of the measurement from the information available. In practice, the uncertainty can be higher due to systematic effects.

2.2 Setting

In this report, we explore the particular problem where two spectra are available ($N = 2$) and we are attempting to distinguish between two possible different materials by finding the areal density of those two specific materials in each pixel of our radiograph.

We are examining the case of the X-ray radiation from a betatron with 7.5 MeV endpoint energy collected by a Varex 4343HE detector as it passes through slabs of various materials, shown in Table 1. Dual energy measurements are acquired by measuring with an unfiltered spectrum and the spectrum when the beam is filtered by 1.905 cm of tungsten. We also examine the possibility if using a spectrum with a lower betatron energy, in this case with a 4 MeV endpoint. In practice the overall exposure from the betatron X-rays is reduced by an order of magnitude when the endpoint is lowered from 7.5 MeV to 4 MeV; we will examine both the impact of 4 MeV endpoint spectra both with the same exposure and with the exposure reduced by a factor of 10.

Table 1. Slab composition and thickness.

Material	Thickness (cm)	Thickness (inch)	Density (g/cm^3)
High density polyethylene	5.3975	2 1/8	1
High density polyethylene	10.795	4 1/4	1
Aluminum	2.54	1	2.7
Aluminum	5.08	2	2.7
Steel	0.635	1/4	7.874
Steel	1.905	3/4	7.874
Tungsten	0.635	1/4	19.254
Tungsten	1.905	3/4	19.254

2.3 Variance

Knowledge of the variance of a measurement is important to finding $\mathcal{F}$.

In a FY24 measurement campaign at ORNL, the above setup was used to acquire radiographs of various slabs and objects under various collimation conditions. Typically, individual exposures lasted 4 seconds, and 75 exposures were averaged together for one frame. Given that multiple measurements were made of the same scene, this allows us to extract the variance of a given pixel under the same conditions across the range of measurements.

We used a set of images, exposures 20 through 75, of a flat field exposure. Exposure 20 is shown in Figure 1, below. For each pixel the variance σ^2 can be determined from the individual pixel exposure values v via $\sigma^2 = \langle (v - \langle v \rangle)^2 \rangle$ where angle braces $\langle \cdots \rangle$ represent the expectation value as averaged over the 55 sample exposures. The resulting set of data can be used to produce a fit of the expected variance of a pixel value as a function of its measured value.

Fluctuations in source intensity cause a systematic change to all the pixels in a given image. Such variation at a single pixel will produce a quadratic dependence of the variance on the mean as opposed to the expected linear dependence for statistically expected data. Consequently, all the images were corrected for exposure by normalizing them all to the same overall brightness (defined by summing the values of all pixels for each image).

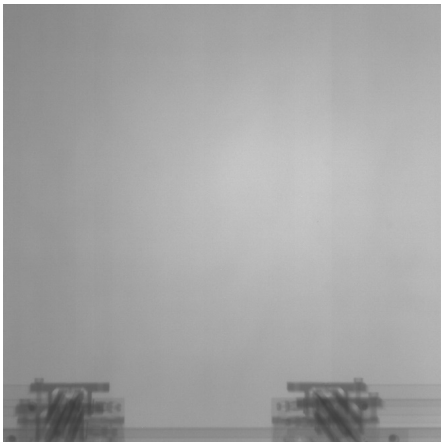


Figure 2. A representative exposure of the set of exposures used to measure the variance.

The detector had previously been characterized to locate bad pixels; these were excluded from the analysis. The mean and variance of all other pixels was determined. The best fit for the variance is

$$\sigma^2 = 0.000010794\, v^2 - 3.62032\, v - 14114.8 \qquad (2)$$

and is shown in Figure 3.

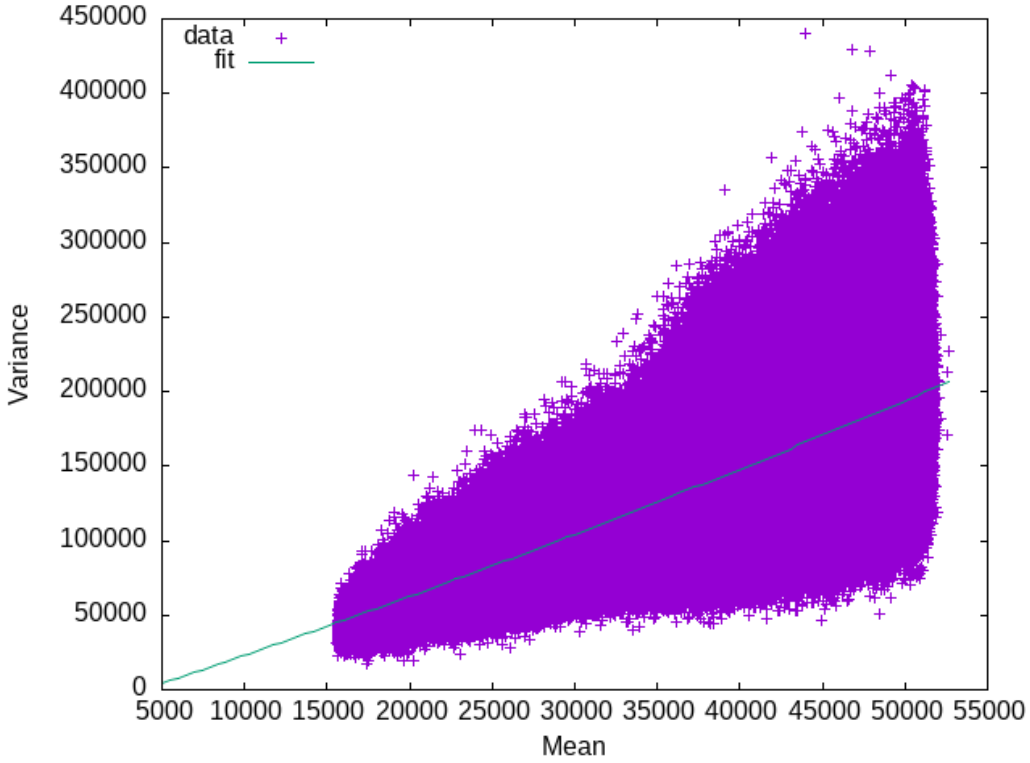


Figure 3. Mean and variance of pixel values from all good pixels of the exposure sequence (purple crosses) with the fit function shown as a green line.

2.4 Spectrum and Response Function

The spectral intensity from the betatron at 7.5 MeV endpoint energy $S_1(\omega)$ and the response function $\epsilon(\omega)$ of the detector had previously been determined. The product of the unfiltered spectrum and efficiency is normalized to 42746 counts and a dark current of 6003 counts, based on previous betatron measurements.

The spectrum behind the tungsten filter $S_2(\omega)$ was estimated using Beer-Lambert attenuation

$$S_2(\omega) = S_1(\omega)\exp[-\mu_W\, x_2\, \rho_W]$$

where μ_W is the mass attenuation coefficient for tungsten (taken from the NIST X-ray attenuation database), $x_2 = 1.095$ cm is the thickness of the tungsten filter, and $\rho_W = 19.254$ g/cm^3 is the density of tungsten.

Figure 4 shows the spectral shapes normalized to unit intensity. The efficiency is shown in Figure 5.

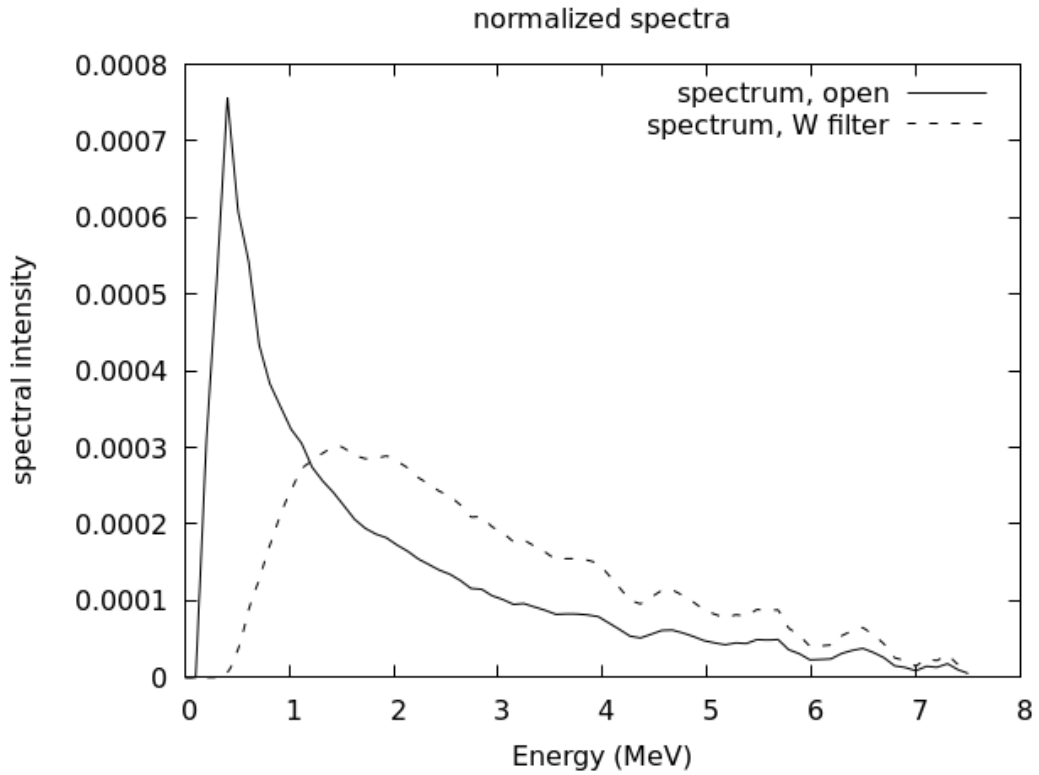


Figure 4. Betatron X-ray spectra normalized to unit weight with 7.5 MeV endpoint energy, with and without filtering.

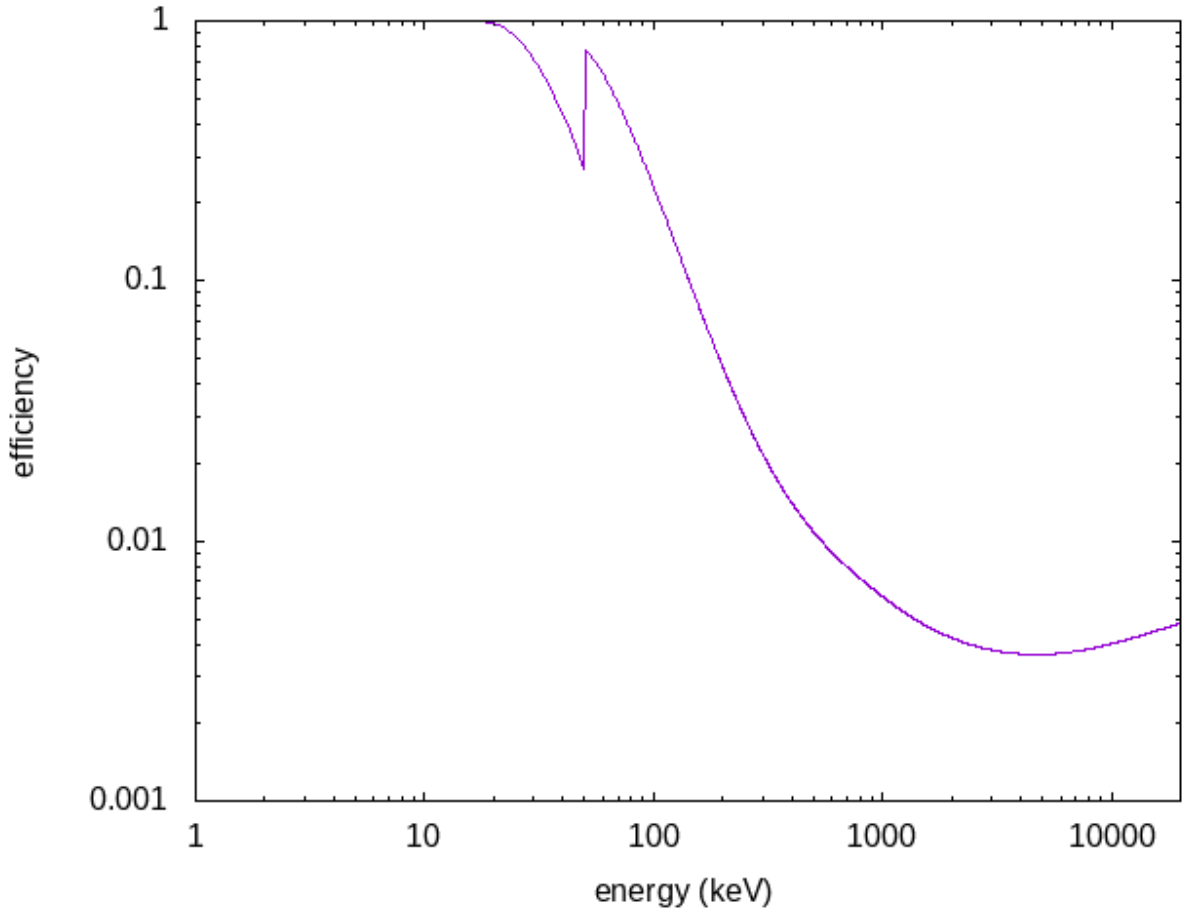


Figure 5. Efficiency of the detector.

2.5 Constructing the information matrix

We assume that material blocks attenuate the incident X-rays according to the Beer-Lambert law. The measured intensity behind block a from spectrum i is then

$$I_{i,a} = D + \int d\omega \; S_i(\omega)\, \epsilon(\omega) \; \exp[-\mu_a \, \lambda_a]$$

where $D = 6003$ is the dark field count. The signal variance of this measurement is computed with Equation 2.

The derivative with respect to the areal density of some additional infinitesimal contribution of material α is then

$$\frac{\partial I_i}{\partial \lambda_\alpha} = -\int d\omega \; S_i(\omega)\, \epsilon(\omega)\, \mu_\alpha \; \exp[-\mu_a \, \lambda_a].$$

Both integrals are carried out with trapezoidal integration over the energy grid determined by the data points used for the spectrum, with other values interpolated onto that grid using log-log interpolation. The mass attenuation coefficients μ_α are from the NIST X-ray attenuation database and are shown in Figure 6.

The derivative of the variance with respect to the additional contribution of this material is

$$\frac{\partial \sigma_i^2}{\partial \lambda_\alpha} = \frac{\partial \sigma_i^2}{\partial I_i} \frac{\partial I_i}{\partial \lambda_\alpha}.$$

When this is combined with Equation 2, we have all the information needed to evaluate Equation 1.

Note that the vectors in the space of materials $\partial I_i / \partial \lambda_\alpha$ and $\partial \sigma_i^2 / \partial \lambda_\alpha$ are proportional to $\partial \sigma_i^2 / \partial I_i$ which is independent of the material index. A consequence of this is that the range of $\mathcal{F}$ is the vector space spanned by the N vectors $\partial I_i / \partial \lambda_\alpha$. With only have two spectra, the dimensionality of the problem is two and trying to fit to more than two materials leads to a singular $\mathcal{F}$ matrix.

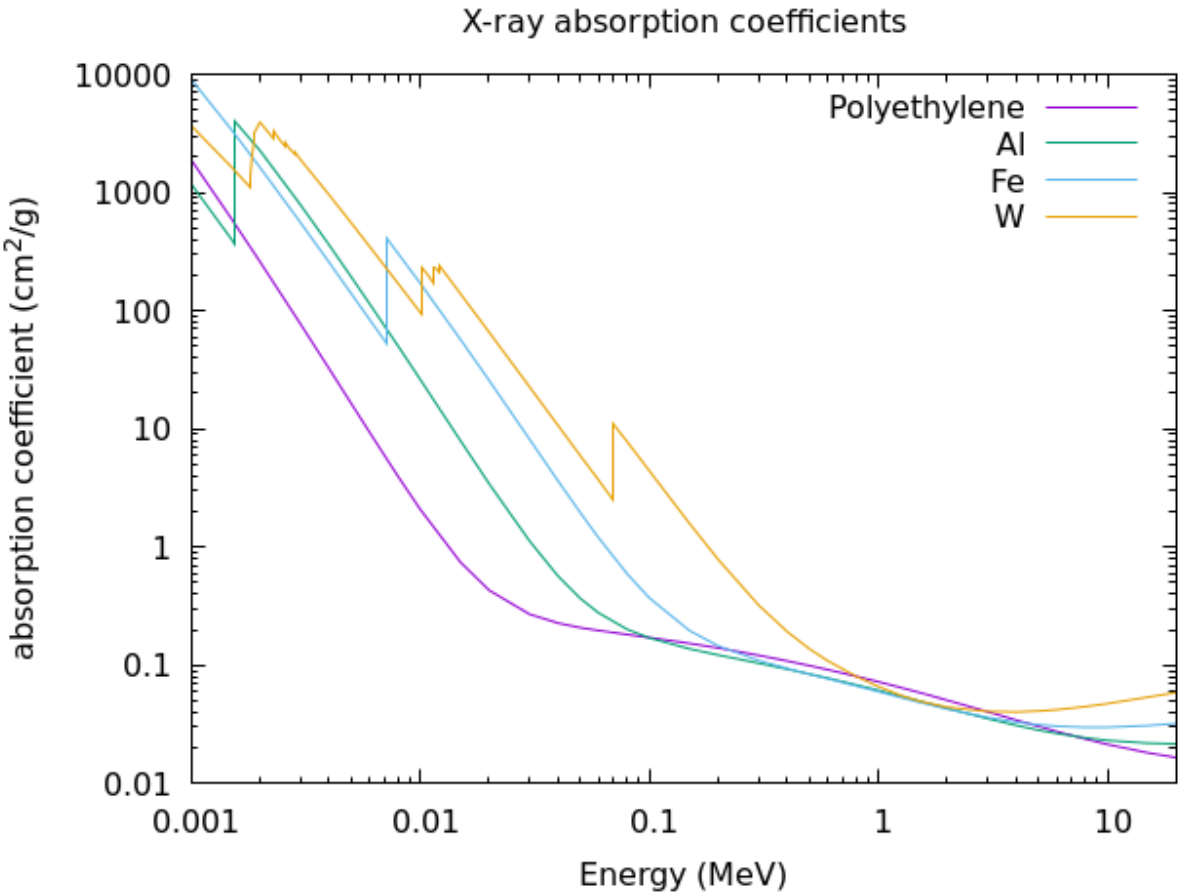


Figure 6. The mass attenuation coefficients of the four materials used.

2.6 Calculation Set 1: Basic Material Discrimination

For each sample slab in Table 1, the signal was computed for the filtered and unfiltered experimentally determined 7.5 MeV endpoint spectra. For this set of spectra, we hypothesize that the slab could be composed of two candidate materials (chosen from polyethylene, aluminum, steel, and tungsten) and quantify the lower limits on uncertainty of any attempt at material reconstruction using these two materials by computing and inverting $\mathcal{F}$.

2.6.1 Results

The full results are shown in Appendix A, including the uncertainty on material estimates, the condition of the matrices, and the lower bound covariance matrix $\mathcal{F}^{-1}$.

2.6.2 Discussion

We see a general trend that it is difficult to distinguish between low and medium Z (atomic number) materials in this data set. We choose the criterion that two materials can be distinguished if their uncertainty in areal density is lower than their actual areal density. If the two materials compared contain only polyethylene, aluminum, or steel, the uncertainties are high – frequently significantly much higher than the known areal density – and the condition number of the Fischer and covariance matrices is very high. This is more pronounced when aluminum and polyethylene (the two lowest Z materials) are compared. The covariance matrices show very high anti-correlation between the errors – if the estimate for one measurement is high, the estimate for the areal density of the other material is going to be low by approximately the same amount. This is expected, because if one material has its areal density overestimated the second material will need a lower areal density to return the same measured attenuations. Poorly conditioned matrices indicates that it is difficult to distinguish between the materials – both materials tend to attenuate the X-rays in similar ways – such that the only distinguishable feature is the total material attenuating the signal.

Conversely, when one of the two materials investigated was tungsten, the uncertainties were significantly lower, to the point that the uncertainties were less than the known areal densities and thus allowing some degree of meaningful measurement. The matrices were significantly better conditioned, as well. This suggests that for the spectra and targets chosen, this setup could distinguish between high- Z and low- or mid- Z material, but not between different low- Z or mid- Z materials.

An illustration of this is shown in Figure 7, where the mass attenuation coefficients are plotted with the normalized spectra super-imposed on top. Over the spectral range of the incident X-rays, the X-ray attenuation coefficients for polyethylene, aluminum, and steel are all nearly identical, consisting mostly of a nearly flat Compton scatter region of the attenuation spectrum, while that of tungsten shows notable differences in the form of significant photoabsorption at lower energies and some pair production at high energies. This further confirms the information-theoretic conclusion that we do not expect to be able to distinguish between polyethylene, aluminum, or steel with these spectra.

An exception to this general behavior is when the material slab actually is composed of tungsten. In this case, the uncertainties are relatively high compared to the lower Z materials. This may be because the parts of the spectrum that differentiate tungsten from the other materials is where the attenuation of the tungsten is the highest. Thus, tungsten attenuates out the very parts of the spectrum that distinguish it, making it harder to identify when it is present.

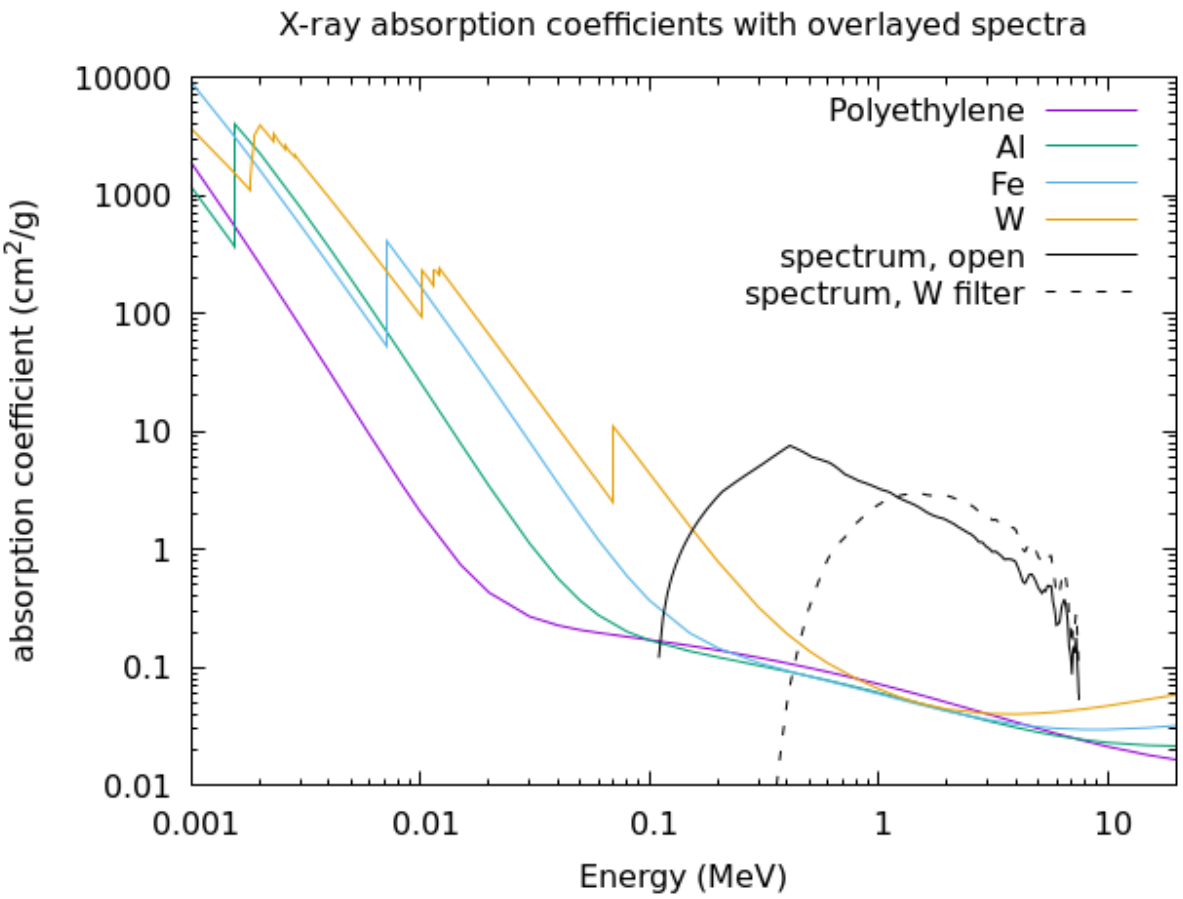


Figure 7. The mass attenuation coefficients of the four materials used, superimposed on the two spectra.

2.7 Calculation Set 2: Effects of Filtration and Choice of Filters

The previous calculation set resulted in tungsten filtering reducing the spectral components specifically useful to distinguish tungsten from the other materials of interest, such that for the tungsten targets the uncertainty in the sectional density from the Cramér-Rao lower bound could be higher than the known sectional density.

Here, we investigate this further, to see what filtering with different materials of different thicknesses does to impact uncertainty in high-Z measurements. We also test the ability of tungsten filtration to distinguish the materials of tungsten samples of various thicknesses. We use the experimentally determined 7.5 MeV endpoint betatron spectrum.

In Figure 8, we investigate the ability of different filter thicknesses and materials to discriminate tungsten from aluminum when the target material is 12.2 g/cm^{2}of tungsten. We see that higher Z materials perform best as filters even if the best case scenario only barely has an uncertainty less than the actual value.

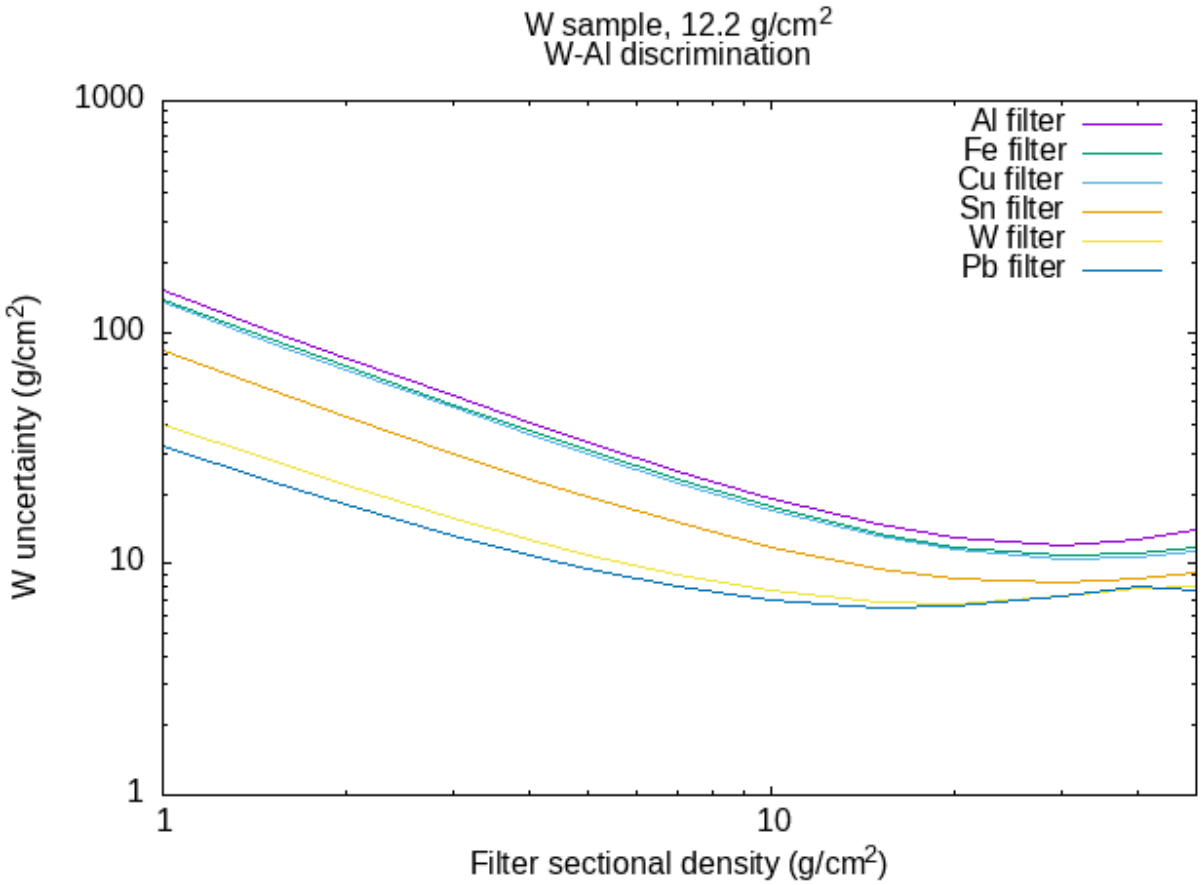


Figure 8. Cramér-Rao lower bound uncertainty distinguishing between tungsten and aluminum, with known 12.2 g/cm^2 tungsten sample, as a function of filter thickness and composition.

In Figure 9, we examine how the thickness of the tungsten target affects our ability to discriminate what it is made of. We see that for thin enough targets and filter thicknesses approximately 10 g/cm^2, the uncertainty can be brought below the actual target thickness and allow some degree of meaningful discrimination.

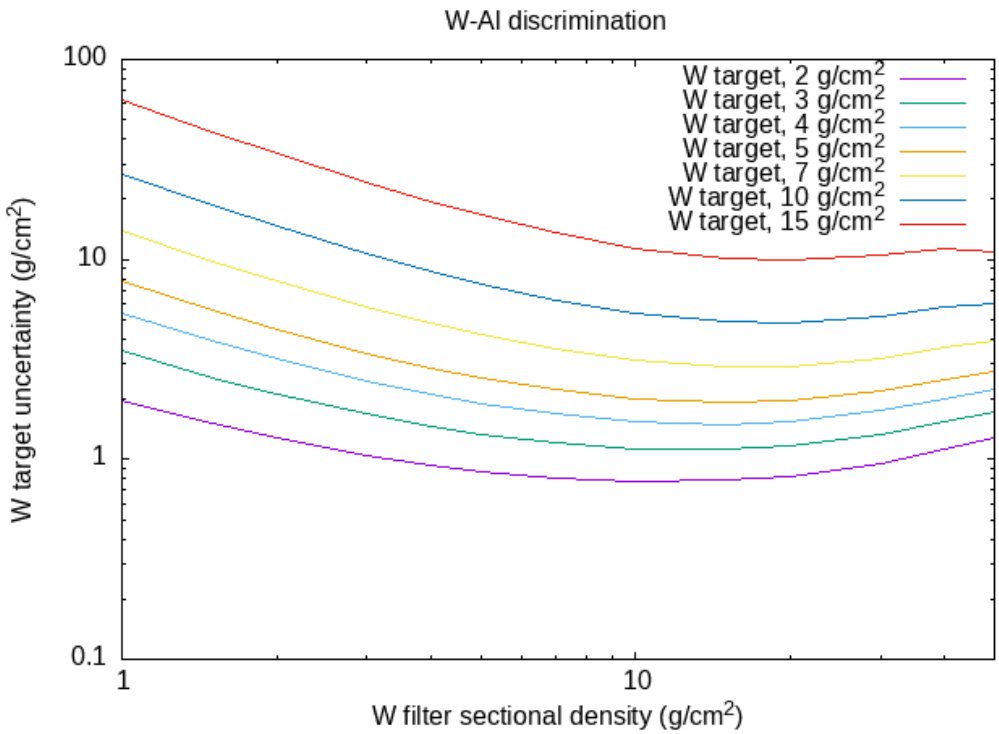


Figure 9. Cramér-Rao lower bound uncertainty distinguishing between tungsten and aluminum as a function of the thickness of a tungsten filter, for different thicknesses of tungsten objects.

In Figure 10 we examine how different thicknesses of different material filters affects the uncertainty at high/low Z discrimination (in this case, tungsten from aluminum) on the different targets used in the experimental campaign. We see a general trend of higher-Z filters giving better performance, and thick (12.2 g/cm^2) tungsten being difficult to discriminate while lower Z materials, even of similar sectional density, are easier to discriminate.

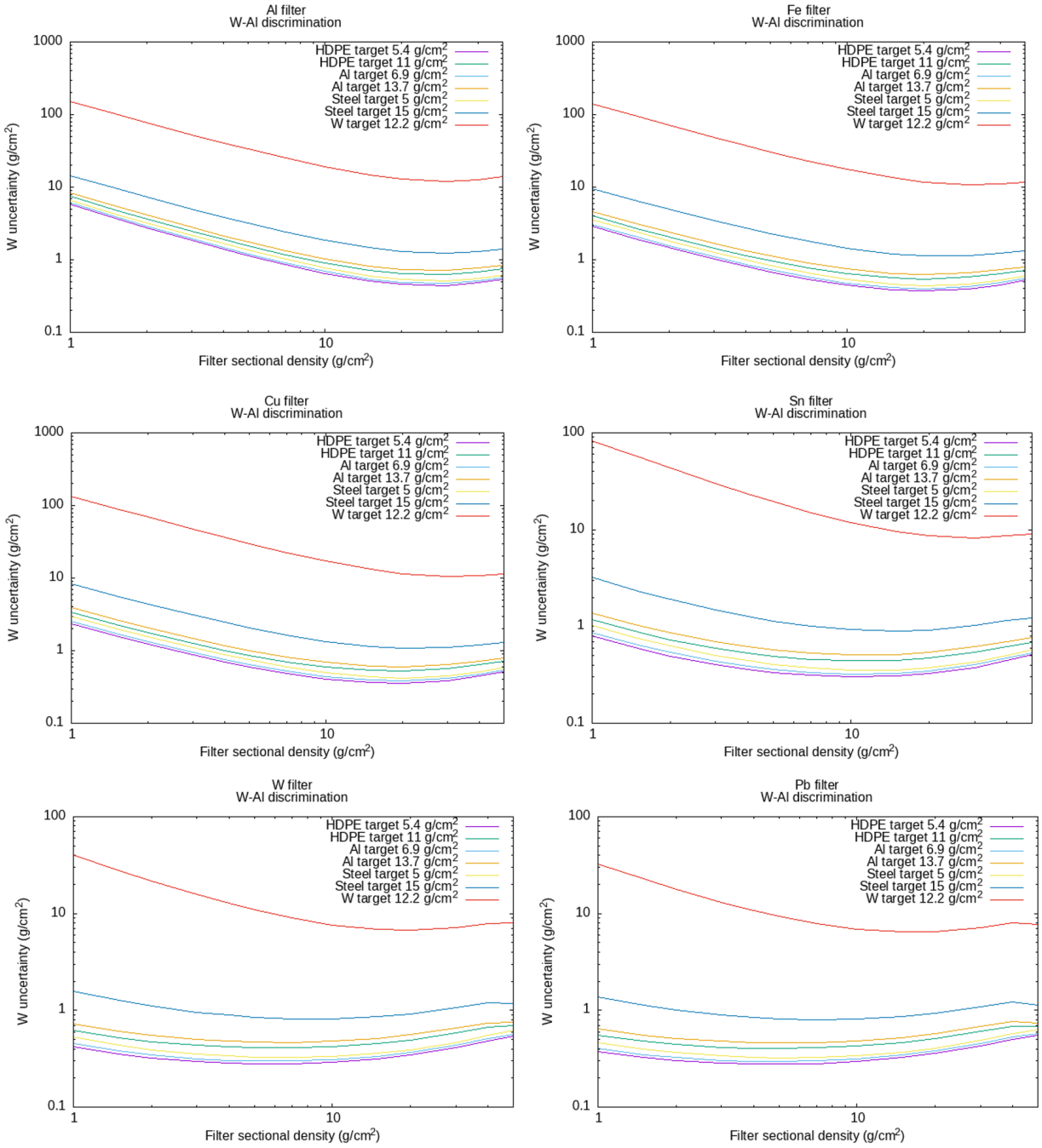


Figure 10. Cramér-Rao lower bound uncertainty distinguishing between tungsten and aluminum as a function of the thickness of filters of different materials, for different targets used in the experimental campaign.

2.7.1 Discussion

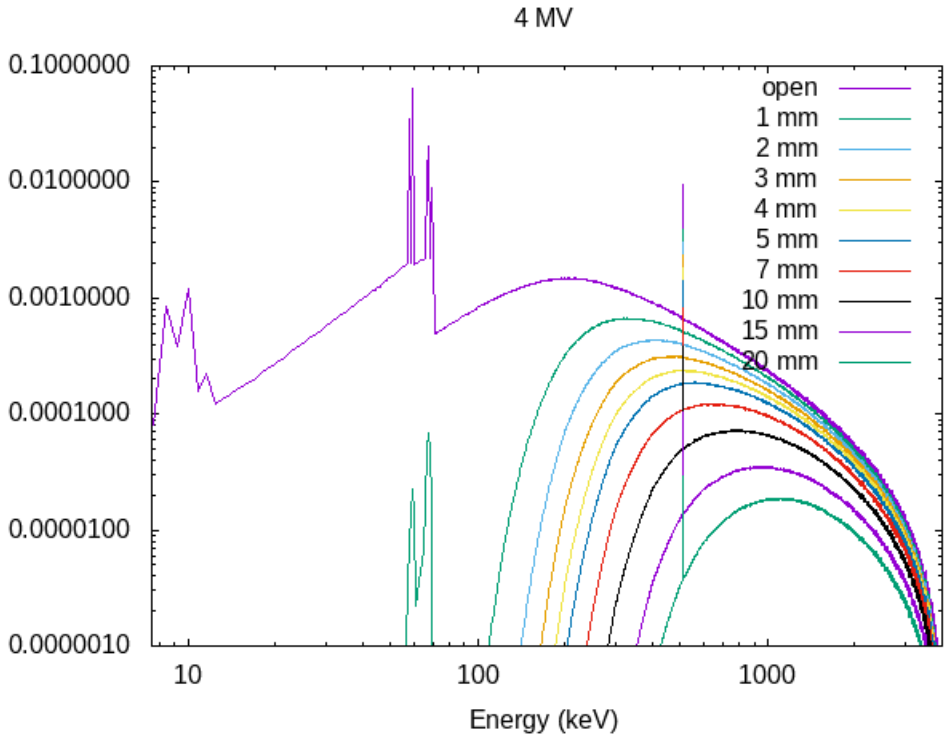
For the particular choice of spectra used in this study, high Z filters are found to generally provide increased discrimination between different materials. We do not see an effect of using the same filter material as one of the materials we are attempting to discriminate compared to other materials of similar Z. As high Z materials attenuate the same part of the spectrum used to

discriminate between high and low Z materials, thick enough high Z materials prove difficult for material discrimination methods in the sense that the spectrum of the radiation that gets past the high Z material does not contain the information needed to distinguish between additional thicknesses of any other material, high or low Z. We find that for the X-ray spectra we used, 10 to 20 g/cm^2 of a high Z filter gives the best ability to distinguish between a high and low Z material when the high Z material is actually present.

2.8 Calculation Set 3: Spectra With Different Endpoint Energies

2.8.1 Spectra

To compare the 4 MeV and 7.5 MeV endpoint energy spectra, bremsstrahlung spectra from electron beams at these energies were simulated in GEANT4 on a 1 cm thick tungsten anode at 45 degrees incidence angle. The spectra are filtered through tungsten of between 1 mm and 20 mm thickness. As before, filtration of these simulated spectra was found analytically using the Beer-Lambert law. To approximate the transmission of the beam through the betatron anode and the various windows and other pieces of matter between the source and the air, the baseline spectra were taken as the spectra filtered by 1 mm of tungsten, which cuts down on the low energy X-rays which we know are not present. These spectra are shown in Figure 11. The detector efficiency is the same as in previous calculation sets.



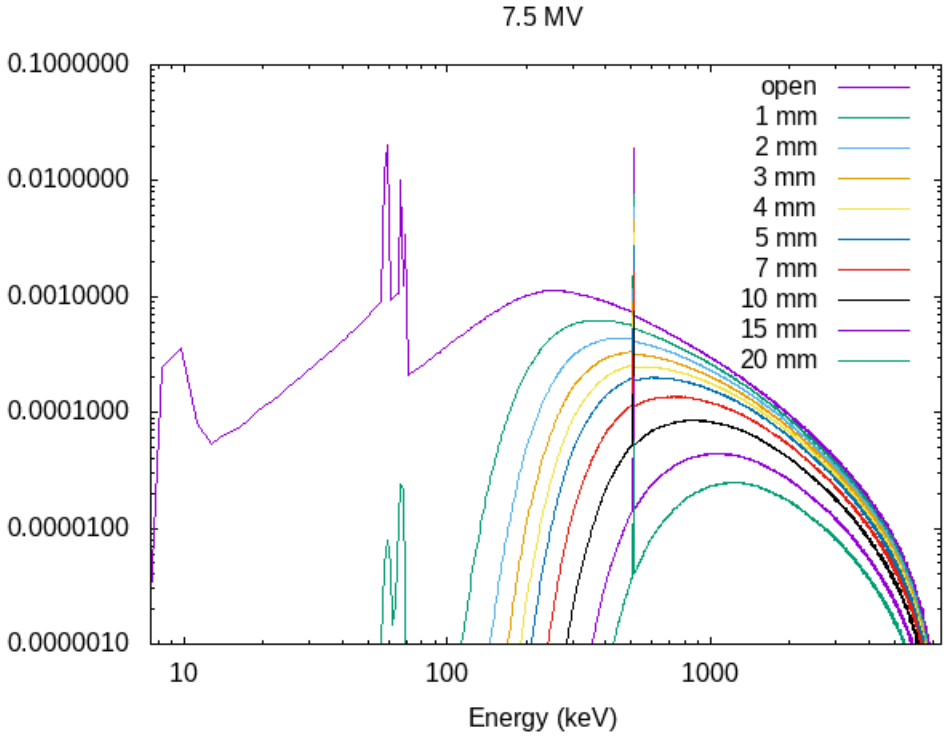


Figure 11. Normalized photon spectra grouped by endpoint energy with different tungsten filter thickness.

To determine the signal and the variance, the baseline 7.5 MeV spectrum was normalized to a pixel grey value of 42764 and an assumed dark count of 6233 was added to the spectral signal. Because the betatron operating at lower energies produces lower intensity X-rays, we approximated the achievable spectrum at 4 MeV endpoint by normalizing it to a pixel grey value of 4276.4 with the same dark count of 6233.

2.8.2 Procedure

Dual energy spectra were found after passing through a target consisting of either the 1 inch aluminum, 2 inches aluminum, or ¼ inch tungsten slabs. One of the spectra was chosen from the set with 1 mm filtration. The other spectrum was either from the same endpoint energy but a thicker filter or from a higher endpoint energy with any of the filters. The spectrum was attenuated through the target analytically using Beer-Lambert attenuation, adjusted for detector efficiency, and the spectrum integrated to get the detector signal.

2.8.3 Results

The material thickness uncertainties are shown in Figure 12 for the 1” aluminum slab, in Figure 13 for the 2” aluminum slab, and in Figure 14 for the ¼” tungsten slab. In these figures, the 4 MV spectrum is at the reduced intensity compared to the 7.5 MV spectrum we would expect from the betatron.

Similar results for the material thickness uncertainties when the 4 MV spectrum has the same signal as the 7.5 MV spectrum are shown in Figure 15 for the 1” aluminum slab, in Figure 16 for the 2” aluminum slab, and in Figure 17 for the ¼” tungsten slab.

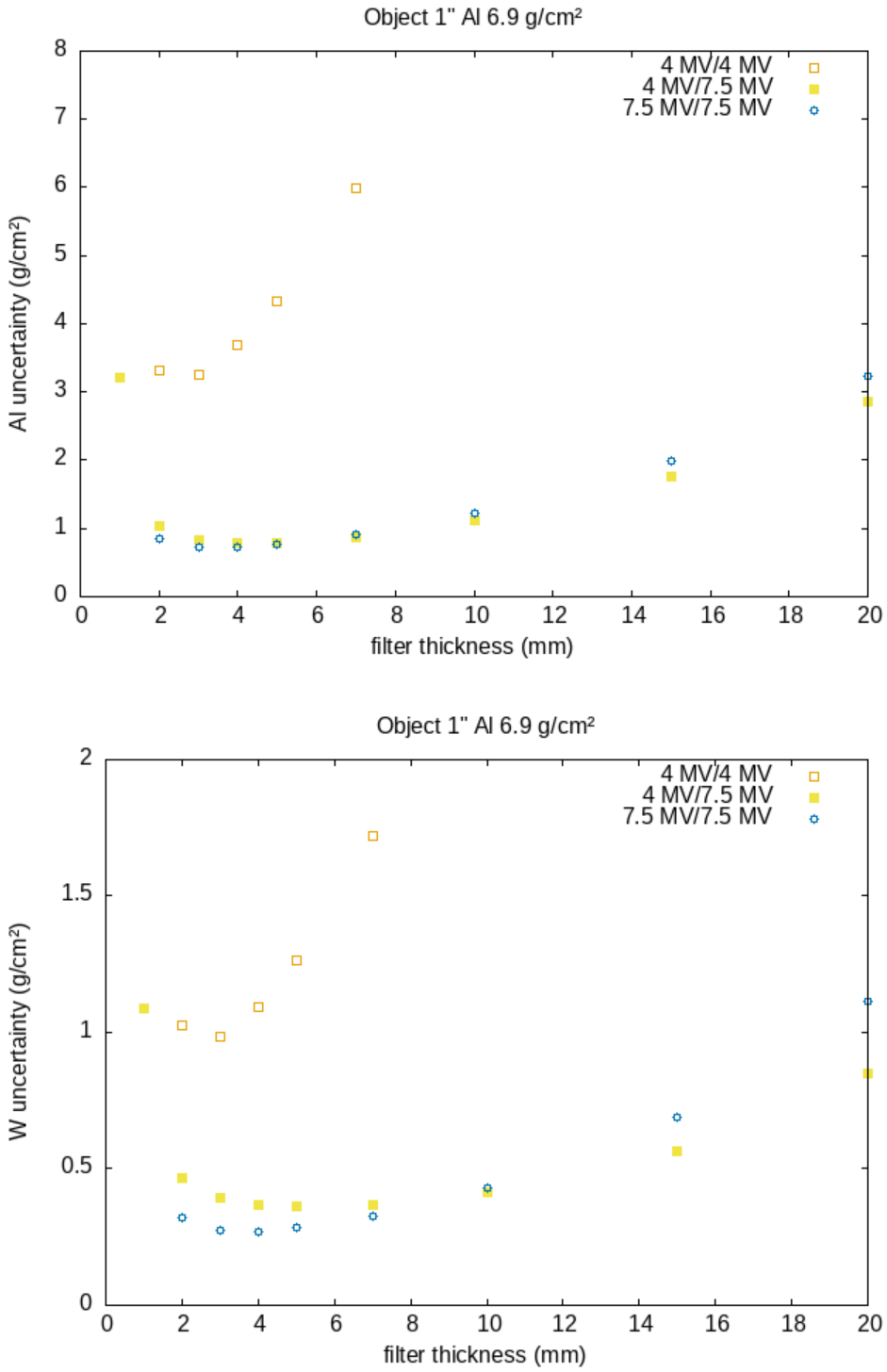


Figure 12. Uncertainly of aluminum (top) and tungsten (bottom) measurements of a 1 inch aluminum slab, for dual-energy measurements using the 4 MV/4 MV (open orange squares), 4 MV/7.5 MV (filled yellow squares), or 7.5 MV/7.5 MV (open orange squares) spectral pairs. The filter thickness is the thickness of tungsten for the second listed spectrum; the first spectrum is always filtered with 1 mm tungsten.

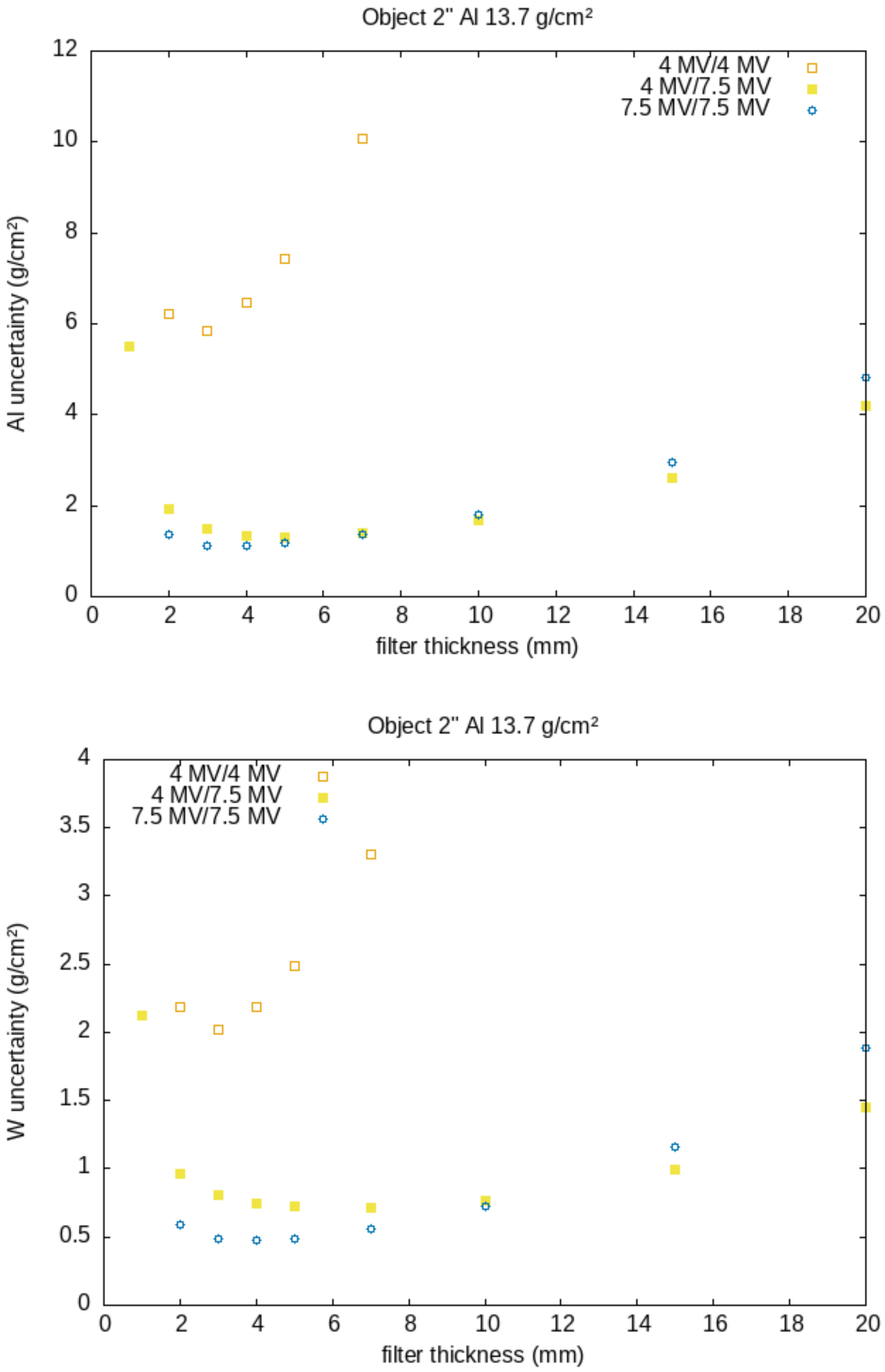


Figure 13. Uncertainly of aluminum (top) and tungsten (bottom) measurements of a 2 inch aluminum slab, for dual-energy measurements using the 4 MV/4 MV (open orange squares), 4 MV/7.5 MV (filled yellow squares), or 7.5 MV/7.5 MV (open orange squares) spectral pairs. The filter thickness is the thickness of tungsten for the second listed spectrum; the first spectrum is always filtered with 1 mm tungsten.

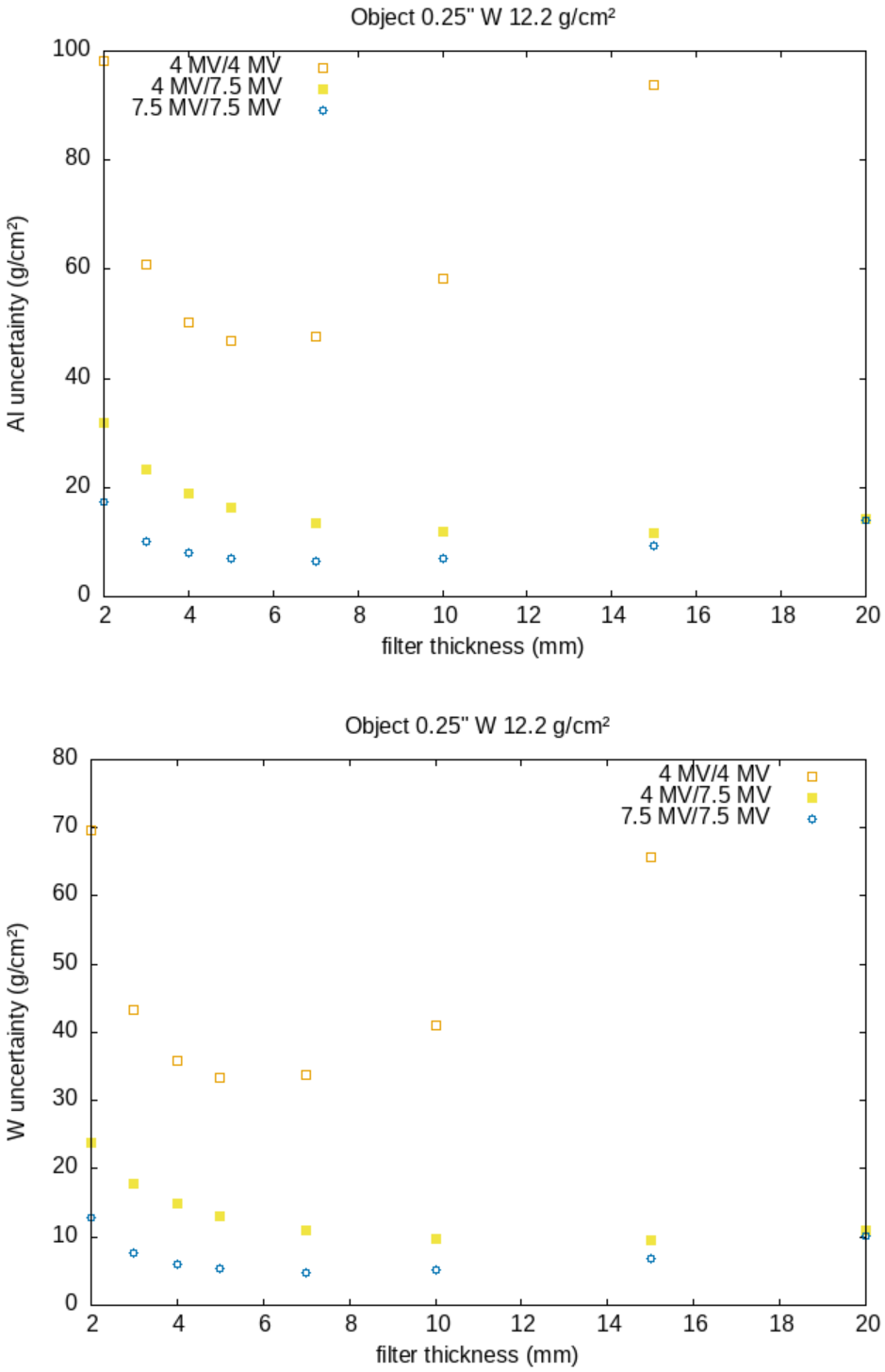
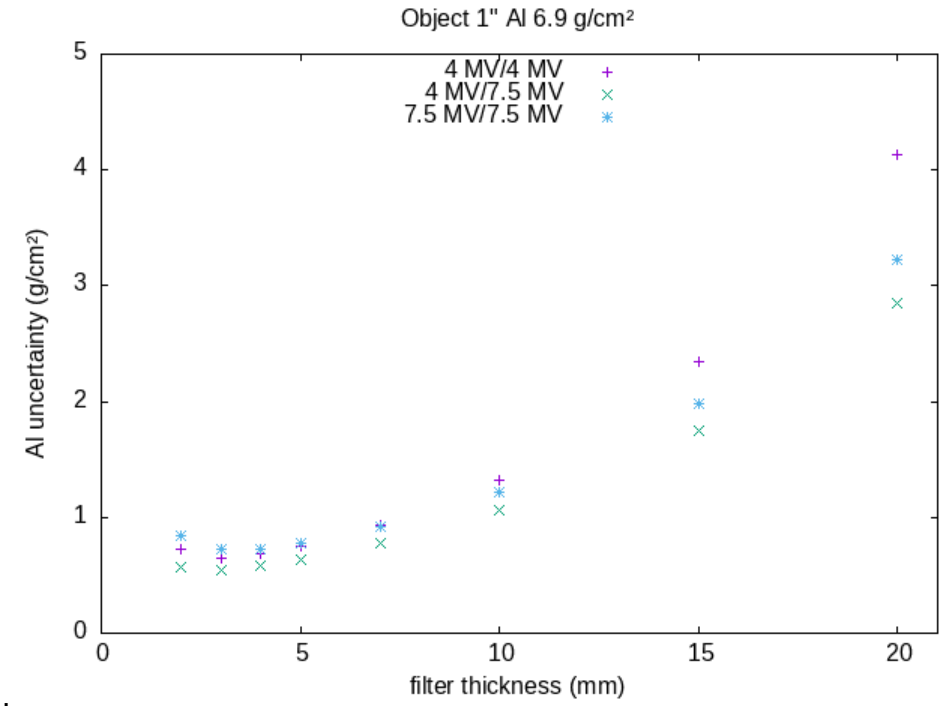


Figure 14. Uncertainly of aluminum (top) and tungsten (bottom) measurements of a ¼ inch tungsten slab, for dual-energy measurements using combinations of the 4 MV and 7.5 MV beams. The 4 MV source is scaled to give 1/10th the signal of the 7.5 MV source. The filter thickness is the thickness of tungsten for the second listed spectrum; the first spectrum is always filtered with 1 mm tungsten.



.

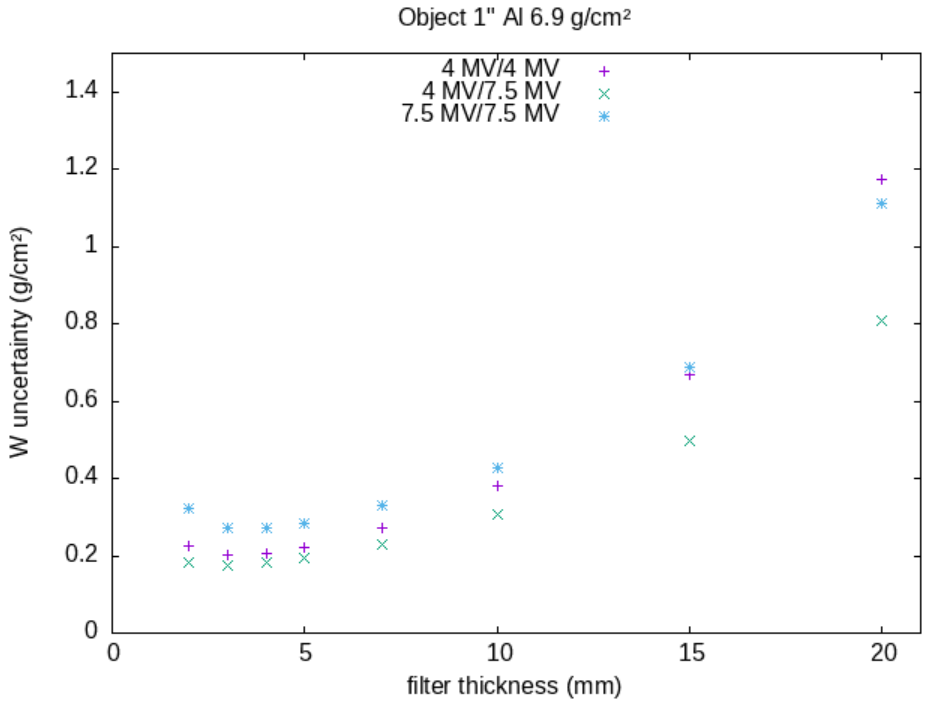


Figure 15. Uncertainly of aluminum (top) and tungsten (bottom) measurements of a 1 inch aluminum slab, for dual-energy measurements using combinations of the 4 MV and 7.5 MV beams, when the 4 MV spectrum gives the same signal as the 7.5 MV spectrum. The filter thickness is the thickness of tungsten for the second listed spectrum; the first spectrum is always filtered with 1 mm tungsten.

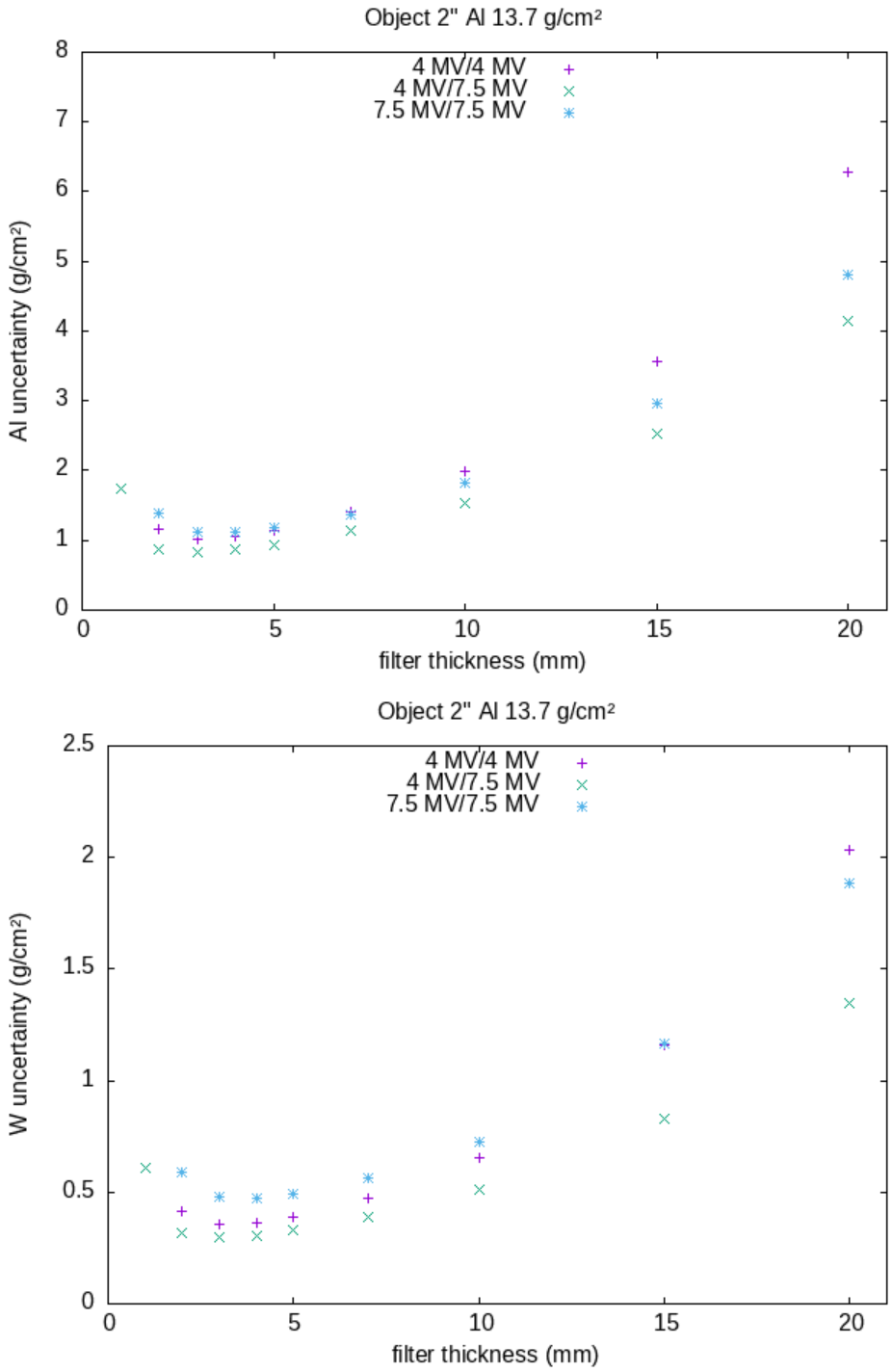


Figure 16. Uncertainly of aluminum (top) and tungsten (bottom) measurements of a 2 inch aluminum slab, for dual-energy measurements using combinations of the 4 MV and 7.5 MV beams, when the 4 MV spectrum gives the same signal as the 7.5 MV spectrum. The filter thickness is the thickness of tungsten for the second listed spectrum; the first spectrum is always filtered with 1 mm tungsten.

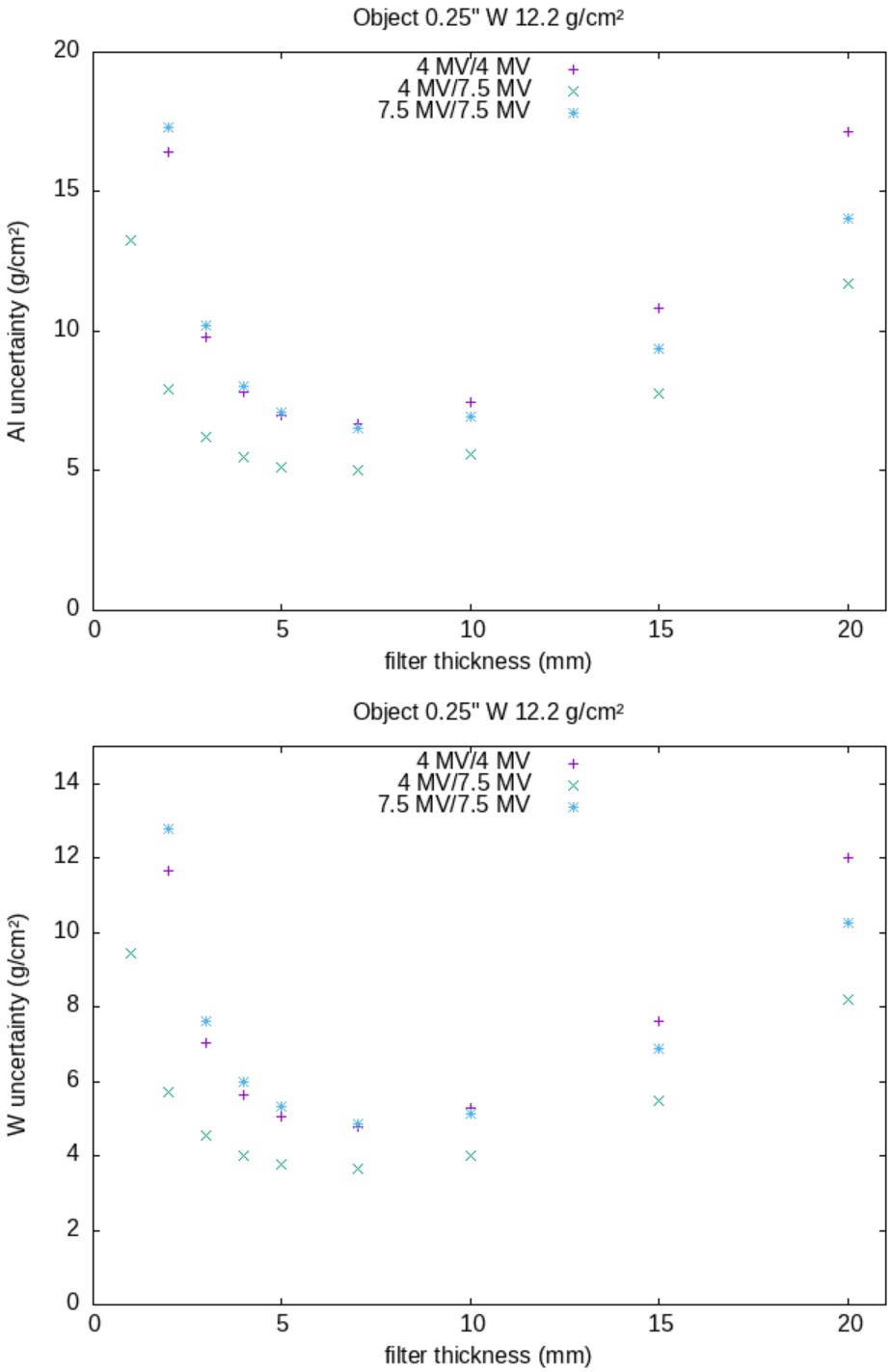


Figure 17. Uncertainly of aluminum (top) and tungsten (bottom) measurements of a ¼ inch tungsten slab, for dual-energy measurements using combinations of the 4 MV and 7.5 MV beams, when the 4 MV spectrum gives the same signal as the 7.5 MV spectrum. The filter thickness is the thickness of tungsten for the second listed spectrum; the first spectrum is always filtered with 1 mm tungsten.

2.8.4 Discussion

If we could produce a 4 MV X-ray beam with the same intensity as a 7.5 MV X-ray beam, using the open 4 MV beam and a 7.5 MV beam with several millimeters of tungsten filtration would allow for improved material discrimination. However, due to the reduced intensity of the X-rays when the betatron is set to 4 MeV, we are unlikely to see these benefits in practice.

These results reinforce the fact that the information matrix reflects the statistical information available in the measurement. Lower signals result in worse signal to noise ratios, and consequently higher uncertainty to the measurements. Therefore, increasing the source intensity or exposure time can help to reduce uncertainties on your material composition up until reaching limits set by systematic effects, accuracy of system model, or algorithmic constraints.

2.9 Calculation set 4: Material Discrimination Over the Entire Periodic Table

We have previously shown that with the spectra we used, we can distinguish high Z materials from low and mid Z materials, but we cannot tell low and mid Z materials apart. We now wish to look into what materials could be meaningfully distinguished with these spectra.

2.9.1 Procedure

The lower bound uncertainties were found for two slabs of steel (assumed elemental iron for this problem) of different thicknesses given the assumption that there are two possible materials in the problem, one of which is iron. The other material is systematically varied across the periodic table from atomic numbers Z = 1 to Z = 92 (excluding iron, Z = 26, as that gives no useful information and is mathematically singular). We used the experimentally-determined spectrum for the betatron at 7.5 MeV endpoint both open and filtered through 1.9 cm of tungsten as the two spectra for the dual-energy measurements.

2.9.2 Results

In Figure 18, we show the uncertainty of discriminating the amount of iron in two steel slabs of different thickness against all other naturally occurring (and a few synthetic) elements in the periodic table with atomic numbers from Z = 1 to 92. We see that in both cases no meaningful discrimination can be achieved for atomic numbers of $Z \lesssim 40$ (Zr) where the uncertainty is larger than the known thickness of iron, and for $Z \gg 40$ the slabs uncertainty in the slab composition becomes low enough to make meaningful conclusions about the slab composition.

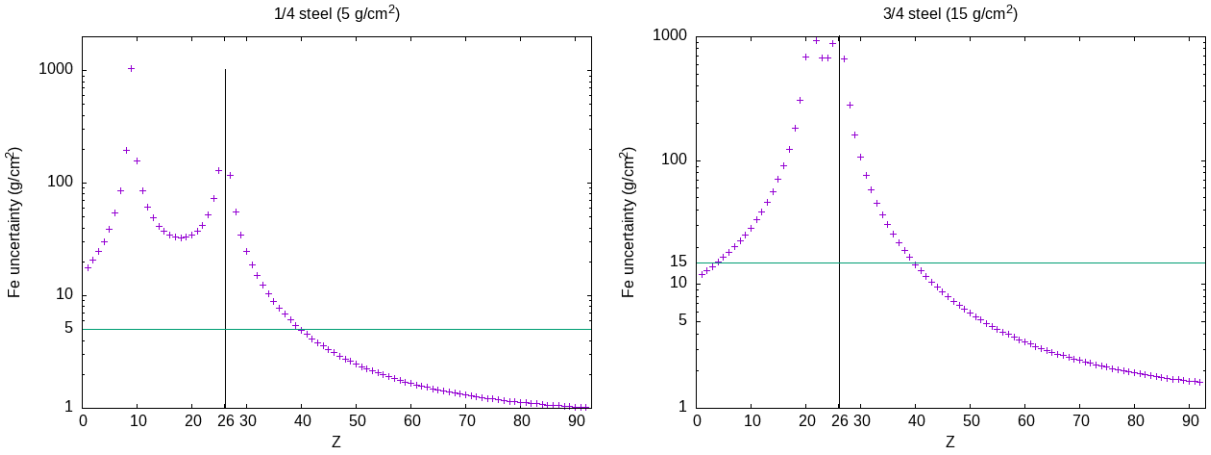


Figure 18. The lower bound to uncertainty for discriminating iron from any other element in the periodic table (listed by atomic number Z in the x-axis), for two steel slabs (assumed pure iron for this exercise) of different thicknesses. The position of Z=26 for iron is marked with a vertical black line. The actual thicknesses of the slabs are marked with a horizontal green line.

2.9.3 Discussion

First, it is worth noting that the lower bound on the uncertainty is a statistical measure. We made certain assumptions about the signal that we measure from our spectra; increasing the X-ray intensity or taking longer exposures will increase the signal and thus the statistical signal to noise ratio and the uncertainty will decrease. Thus, while we can say that for this particular experimental setup we cannot distinguish iron from any element lower in atomic number than zirconium, it is not correct to claim that in general steel cannot be distinguished from other elements until you get to higher atomic number than zirconium. It will depend on the nature of the experiment.

However, we can draw meaningful conclusions about the trends that can be expected in attempts of experimental discrimination of this nature. Namely that in general it will be easier to distinguish high Z from low Z materials, and that distinguishing between mid and low Z materials is likely to be challenging. It is tempting to think that with enough statistics (intense enough sources, long enough exposures) any two materials could be distinguished. However, there are systematic effects which will be challenging to include (for example, estimating the scatter environment, getting sufficiently accurate measurements of the true spectrum and detector response, or the innate ability of a material discrimination algorithm to distinguish materials even in the face of perfect statistics) that will in turn pose significant challenges for discrimination of similar atomic number materials even with high statistics measurements.

A curious feature that is immediately apparent in the graphs of Figure 18 is that in addition to the expected singularity at Z = 26, there is a second singular point for Z < 26 for which mathematically there is no information at all on composition and which depends on material thickness. It is worth delving into this mystery to see if we can better come to terms with what the mathematics is telling us.

In examining the contributions to the Fischer information matrix (Equation 1), the second sum (dealing with the uncertainty in the variance) is found to be negligible compared to the first term (which handles the uncertainty in the signal). If we ignore the second sum, the information matrix for the case of two spectra 0 and 1 and two materials α and β becomes

$$\mathcal{F}_{\alpha\beta} = \frac{1}{\sigma_0^2}\frac{\partial I_0}{\partial \lambda_\alpha}\frac{\partial I_0}{\partial \lambda_\beta} + \frac{1}{\sigma_1^2}\frac{\partial I_1}{\partial \lambda_\alpha}\frac{\partial I_1}{\partial \lambda_\beta}.$$

Each of the two terms is an outer product. We can immediately see that if $\frac{\partial I_0}{\partial \lambda_\alpha} \propto \frac{\partial I_1}{\partial \lambda_\alpha}$, $\mathcal{F}_{\alpha\beta}$ itself becomes an outer product with matrix elements $\mathcal{F}_{01} = \mathcal{F}_{10} = \sqrt{\mathcal{F}_{00}\mathcal{F}_{11}}$ and the determinant $|\mathcal{F}_{ij}| = 0$. A determinant of zero means the problem is singular, F_{ij} cannot be inverted, and the lower bound uncertainty diverges. Thus, it should come as no surprise that if the two materials are the same this condition automatically holds and there is no information present in the measurement that can make the distinction requested.

In our analysis, a singular value decomposition is performed on the information matrix as a prelude to inversion. We find that the two singular values are different by 4 orders of magnitude or more, showing that the matrices are poorly conditioned even for cases where meaningful uncertainties can be extracted.

Now let us examine the case of α = H and β =Fe. The absorption spectra of these two elements are different, so after passing through a significant amount of iron the parts of the spectrum that differentiate the iron are preferentially filtered out. Thus, $\frac{\partial \boldsymbol{I}_i}{\partial \boldsymbol{\lambda}_H}$ will be larger in magnitude than $\frac{\partial \boldsymbol{I}_i}{\partial \boldsymbol{\lambda}_{Fe}}$ for any spectrum i. The difference is more pronounced on the higher energy spectrum.

On the other hand, consider the case where the atomic number is close to iron. For completeness, we can take the ¼ inch slab from Figure 18 and choose the element with the minimum uncertainty between the two singular points, which turns out to be potassium (K). So if we take α = K and β =Fe we find that because these are relatively close in atomic number Z, $\frac{\partial \boldsymbol{I}_i}{\partial \boldsymbol{\lambda}_K}$ also approaches $\frac{\partial \boldsymbol{I}_i}{\partial \boldsymbol{\lambda}_{Fe}}$. However, the difference is more pronounced in the lower energy of the two spectra.

Assuming a smooth variation in $\frac{\partial \boldsymbol{I}_i}{\partial \boldsymbol{\lambda}_{\alpha(Z)}}$ with Z, this indicates that there will be some Z between H and K for which the variations $\frac{\partial \boldsymbol{I}_i}{\partial \boldsymbol{\lambda}_{\alpha(Z)}}$ for the two spectra are the most closely proportional to $\frac{\partial \boldsymbol{I}_i}{\partial \boldsymbol{\lambda}_{Fe}}$. At this point, the information matrix is most closely approximated by an outer product and will be the most poorly conditioned, which in turn will give an element of high uncertainty. For the particular case of ¼ inch steel, this works out to α = F and explains the double peak in the graphs of Figure 18.

2.10 Overall Discussion and Conclusions

The primary spectral intensity for the high energy range we consider occurs in an energy range where Compton scatter dominates and neither photo-absorption nor pair production have a significant contribution to the X-ray absorption for low and mid Z materials. Consequently, any measure of absorption of these materials is determined entirely by the electrons in the X-ray path length for any of the spectra we were able to achieve, and material discrimination is not possible. Different choices for the interrogating spectra (such as working at lower energies where the photoelectric effect is more prominent) could lift this degeneracy and allow improved material discrimination in the low to mid Z range, but at the expense of reduced penetration.

High Z materials show some photo-absorption in the lower spectral range and some pair production in the higher spectral range, allowing the potential to distinguish high Z materials from low and mid Z materials. However, a significant thickness of high Z material in the path length filters out precisely those X-rays that help to distinguish the high Z material such that discriminating between a moderate amount of high Z material with additional low or mid Z material versus a full thickness of high Z material becomes difficult.

We find that the best filter materials for material discrimination are high Z materials such as tungsten or lead. For the spectra used in this test, between 10 and 20 g/cm^2 of filter gave the best ability for material discrimination.

When using a betatron, little advantage was found in using lower energy beams for producing X-ray spectra, if the significantly lower intensity of the X-rays produced with lower energy beams is included as part of the model. This conclusion does not necessarily apply to X-ray spectra produced with other sources; an example with equivalent intensity at 4 MV and 7.5 MV showed slightly better discrimination than comparing filtered and unfiltered 7.5 MV beams.

3.0 Inverse modeling to study material discrimination in dual-energy radiography

Section 2.0 introduced computational methods to study uncertainties expected from unbiased estimators, such as the optimization of a least-squares misfit to determine a most-likely material composition from an object being interrogated. For this and the following sections, we present the physics (forward) model and the inverse model used to determine object composition. This will be used to demonstrate how well materials can be discriminated between and quantified from dual-energy X-ray radiography.

Forward and inverse models have been previously developed as part of previous work [Gilbert, 2016] [Gilbert, 2025] and are reused here for this illustration. These models describe how a spectrum of X-rays is attenuated by an object and how a pixel of an imaging detector observe that spectrum of X-rays. The forward model developed in previous work is essentially that which was introduced in Section 2.0, and is given here again with some slight differences from the previous section:

$$d_{ij}(\vec{\rho}) = \int dE \;\; c(E)\,\epsilon(E)\,[\,\phi_j(E)\;\exp[-\vec{\mu}(E)\cdot\vec{\rho}] + \;\phi_{j,scat}(E)\,] \tag{3}$$

Here, d_i is the observed data for spectrum j and pixel i. As in Section 2.0 the source spectrum $\boldsymbol{\phi_j}$ can be formed by some combination of source endpoint and beam filtration. All source spectra are assumed to be bremsstrahlung, therefore very broad in energy. Scattered radiation, that which has scattered somewhere in its path between the source and detector, is commonly present and captured in the term $\boldsymbol{\phi}_{j,scat}$. The detector efficiency is given by ϵ, which describes the likelihood that the detector will observe an X-ray of given energy. The material attenuation coefficients are given by μ and the areal densities are given by ρ. Note that both μ and ρ are vectors, indicating that there may be more than one material for a given X-ray pathlength. The integral over energy indicates that the detector has no energy selectively and integrates over all energies for a single signal per pixel. The value c is a multiplier that assumes a linear scintillator, i.e., that the scintillation light produced increases linearly with incident X-ray energy.

The inverse problem involves determining a most-likely material composition from some observed data. That is done here simply with a least-squares misfit.

$$\min_{\vec{\rho}} \left\| \vec{d}(\vec{\rho}) - \vec{d}_{obs} \right\|^2 \tag{4}$$

Here, $\vec{d}_{obs}$ is the observed radiography data, a vector here to capture all image pixels. Likewise, the vector $\vec{\boldsymbol{d}}(\vec{\boldsymbol{\rho}})$ captures the physics model for all image pixels and endpoints. For a given set of assumed materials, the optimization of Eq. (4) finds the most likely quantity of the materials in the material set at each image pixel. The methods used here are described in more detail in [Gilbert, 2025]. This inverse model framework will be used in the following sections.

3.1 A simple test of the Cramer Rao lower bound

To test how well the uncertainties estimated from the Cramer Rao lower bound (CRLB) reflect computational uncertainties from the inverse problem in Eq. (4), we generate very simple radiographs using Eq. (3) and complete the inversion. A simple simulated radiograph is shown below in Figure 19, at left. The X-ray attenuation from poly, aluminum, steel, and tungsten slabs were calculated using Eq. (3). No random noise or scatter was included in this section. The thicknesses used for the simulation are the thinner variety of the same materials in Table 1. Using an assumed two material set of [Poly, W] for the inversion algorithm and optimization, the estimated material thicknesses, in g/cm^2, are shown in Figure 19 at center and at right. For the polyethylene estimated thicknesses, notice that it is estimated in the areas where poly, aluminum, and steel are located. This is consistent with the X-ray attenuation of poly being most similar to that of aluminum and steel, whereas tungsten exhibits considerably different X-ray attenuation.

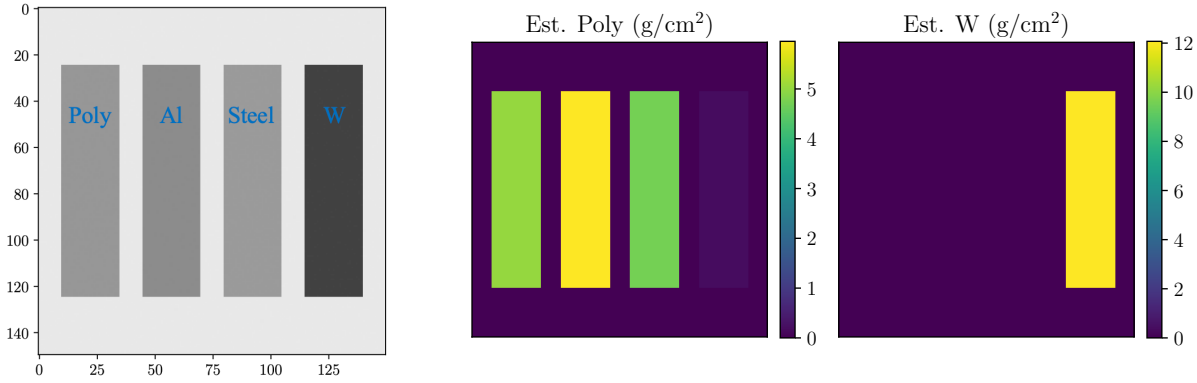
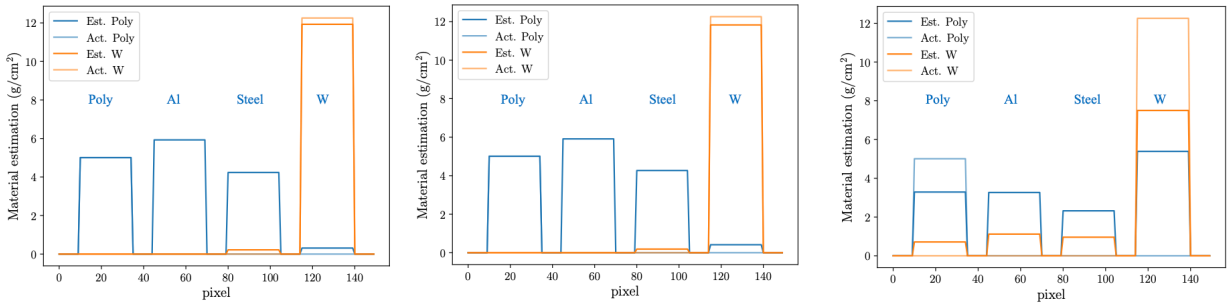


Figure 19. (left) A simple, simulated radiograph of material slabs. (right) Material estimation output for a two-material set of poly and tungsten (W).

Next, we test if the outputs from the inverse algorithm, and any material confusion exhibited, correspond to the values of the CRLB calculation. To do this, we determine the output of the inverse algorithm for different sets of X-ray spectra. From Section 2.0, we learned that the computational uncertainty from estimates from an inverse algorithm vary considerably based on the set of X-ray spectra used. Figure 20 shows a line profile of the material estimates from the simple, simulated X-ray data showing the estimated material thicknesses for three sets of endpoints. This shows that the [7.5 MV, 7.5 MV filtered], and [4 MV, 7.5 MV filtered] spectra pairs perform well, clearly discriminating between low-Z and high-Z materials. In contrast, the [4 MV, 7.5 MV] result shows considerable material confusion, even when no noise is applied to the simple simulated image data.

Table 2 shows the CRLB calculation for the same X-ray spectra pairs. It is seen that the CRLB uncertainty for the spectral pair that performed worse in the inverse algorithm has a higher CRLB value by a factor of 3-5x, indicating a correlation between the two, as expected.



(a) (b) (c)

Figure 20. Line profiles of the material thicknesses estimated for the spectra: (a) [7.5 MV, 7.5 filtered], (b) [4 MV, 7.5 MV filtered], and (c) [4 MV, 7.5 MV]. Actual thicknesses are shown for each material as a lighter shade, to compare to those values estimates.

Table 2. Numerical uncertainties estimated from the Cramer Rao lower bound (CRLB) framework introduced in Section 2.0.

Spectra pair	Poly CRLB uncertainty (g/cm^2)	Tungsten CRLB uncertainty (g/cm^2)
4 MV, 7.5 MV	15.4	13.9
4 MV, 7.5 MV filtered	4.7	4.5
7.5 MV, 7.5 MV filtered	3.6	3.4

3.2 A computational study on the effect of scatter

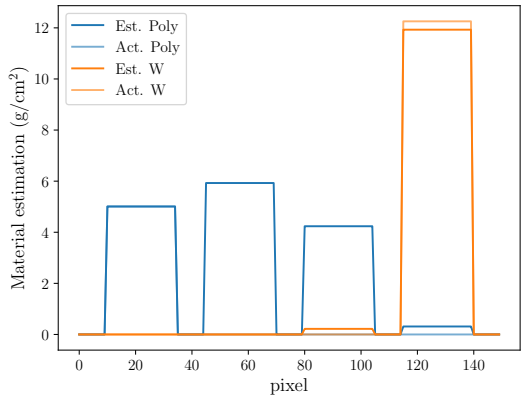
In Section 2.0 the Cramer Rao lower bound considered computational uncertainty from data with random noise and an unbiased estimator of material thicknesses, such as the optimization of a least-squares misfit between observed data and some data model. What this study does not capture is systematic uncertainties. Rather than random noise such as that from counting statistics, systematic uncertainties would capture things like the presence, and the quantity, of scatter in the observed radiography data. Scattered radiation is a significant issue in high-energy radiography as the most likely interaction of an X-ray with matter is scatter, namely incoherent Compton scatter. Scatter can occur in:

- the X-ray source betatron,
- the object being interrogated,
- the surrounding environment of the radiography system, and
- in the X-ray detector medium and materials close to the detector, such as detector shielding and electronics.

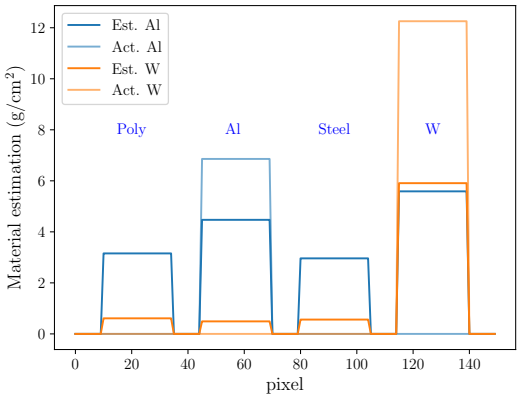
Scatter is difficult to remove [Miller, 2024], or to anticipate in a model [Campbell 2025]. Again using Eq. (3) to produce simple radiography data of the multi-material slabs introduced in the previous section, in this section we add a non-zero contribution of scatter and test the sensitivity of the inverse algorithm to this and how it affects the ability to discriminate between low-Z and high-Z materials. Here the material set for all of the results is [Al, W]. Scatter is denoted as a fraction of the background (unattenuated beam) and is added as a constant over the entire image plane. This simplifies the interpretation of the results.

The results of this study are shown in

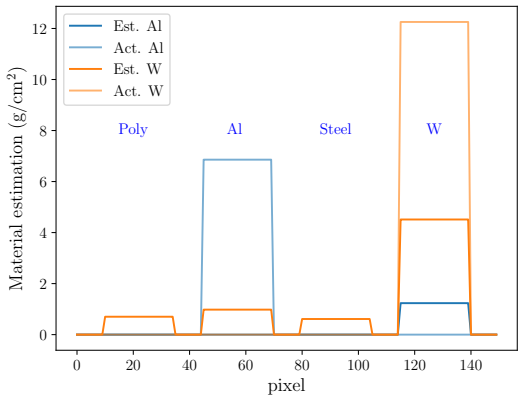
Figure 21, showing a comparison of the actual material estimates to those estimated. Here, the materials assumed in the inverse algorithm are aluminum (representing low-Z) and tungsten (high-Z). In comparing the actual thicknesses simulated to those estimated, it is clearly seen that scattered radiation significantly affects the ability to accurately discriminate between materials and estimate their thickness. Even a modest level of scatter, 5%, causes an underestimate of the tungsten thickness by about 50% and severe confusion between tungsten and aluminum. This indicates a strong sensitivity of inverse algorithms to unknown, or inaccurately modeled, scattered radiation.



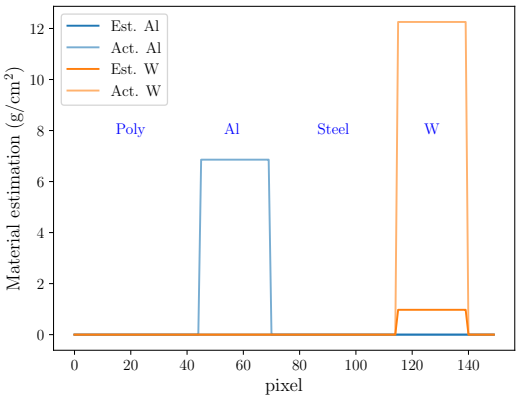
(a) 0% scatter



(b) 5% scatter



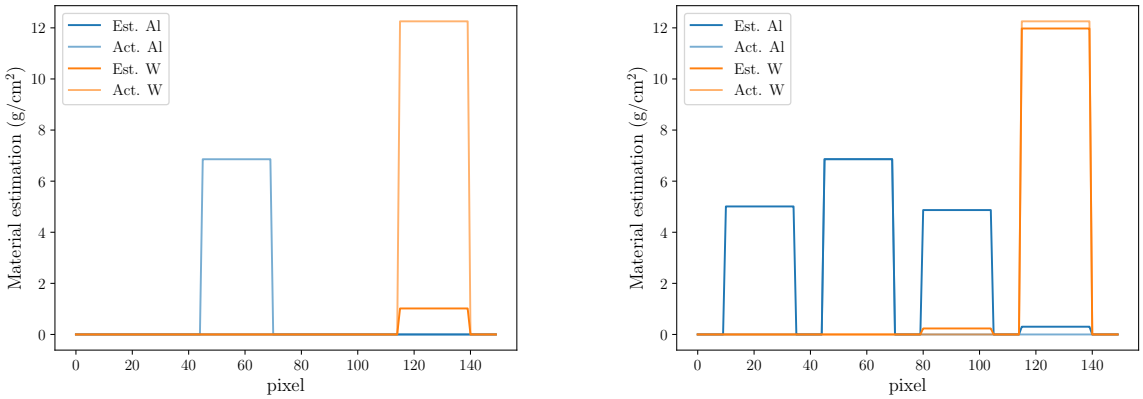
(c) 20% scatter



(d) 50% scatter

Figure 21. Line profiles of the material thicknesses estimated from the inverse algorithm when different levels of scatter are present in the image data, compared to the actual, for a range of scatter levels. The added scatter is a flat profile, percentage of the background, unattenuated regions of the simulated image data.

The results in
Figure 21 did not have the scatter modeled at all in the inverse algorithm. Previous work has shown that scattered radiation can be modeled and removed to reduce this sensitivity when accurate material discrimination and quantification is sought [Campbell, 2025]. Figure 22 shows the result from the inverse algorithm with a significant level of scattered background, 50%, with and without the scatter modeled in the inverse algorithm. In Figure 22b, it is shown that if the scatter is correctly modeled in the inverse algorithm the no-scatter result is recovered, Figure 21b.



(a) 50% scatter, no model (b) 50% scatter, with model

Figure 22. Line profiles of material estimates from the inverse algorithm when a significant portion of the modeled image data is scatter, 50%. (a) Estimates when the inverse algorithm does not include a model of the scatter. (b) Estimates when the inverse algorithm has an accurate scatter model.

Scatter is always present in high-energy radiography data. While collimation can be used to reduce this [Miller, 2024], modeling or computationally removing are also effective [Campbell, 2025]. Any quantitative image analysis should consider the presence of scatter since results will be very sensitive to this.

4.0 Experimental material discrimination

4.1 Experimental data acquisition

To test the ability to complete material discrimination, a data acquisition campaign was completed in FY24. The campaign used a JME PBX7.5M betatron X-ray generator that is capable of producing a bremsstrahlung spectrum of X-rays of up to 7.5 MeV. The objects scanned are single material slabs that were introduced in Table 1. These objects were scanned with two spectra, either through:

- a fully open, unfiltered beam for the lower-energy spectrum and a higher-energy spectrum that had a 3/4" thick tungsten filter, or
- a coarse grid that had interspersed layers of no filtration and 3/4" filtration.

The X-ray detector used was the Varex 4343HE, which has a gadolinium oxysulfide scintillator, active area of 43 x 43 cm, and a 139 µm pixel pitch. For higher energies, the detector employs a 1-mm thick copper layer placed near the scintillator. This reduces the mean energy of the incident beam and creates secondary particles in order to achieve higher efficiencies. To reduce random noise in the data, image data were the average of seventy-five four second acquisitions. The experimental setup is shown in Figure 23.

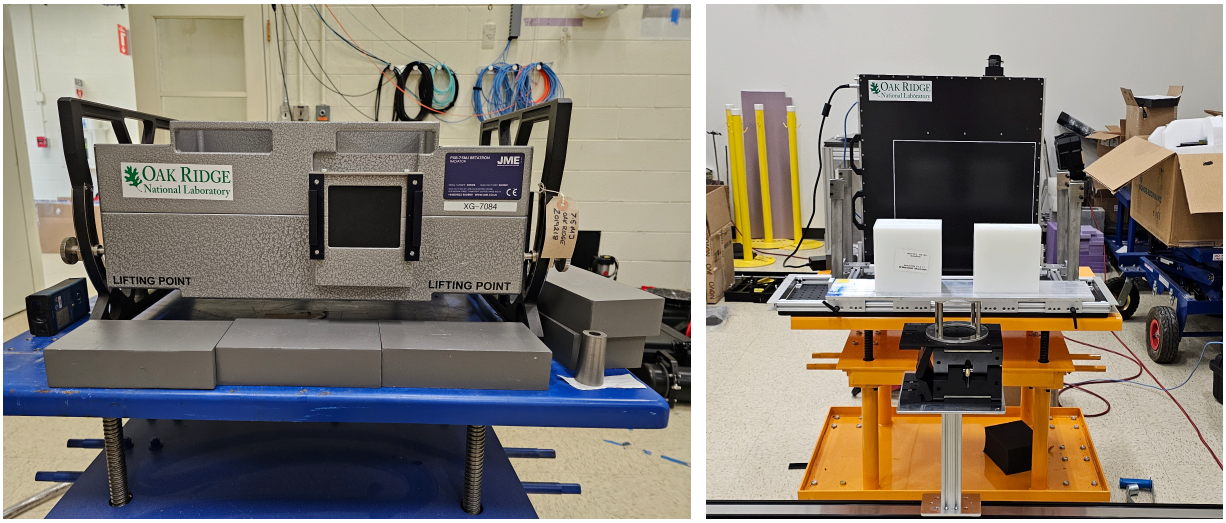


Figure 23. (left) The JME betatron used for the material discrimination experiments. (right) The imaging system, showing the poly material blocks in the foreground and the imaging detector in the background.

4.2 Material discrimination using filtered spectra for dual energy radiography

The inverse algorithm methods given in Section 3.0 can be used to estimate material thicknesses from dual-energy X-ray data. A physical model of the source spectra, object attenuation, and detector response were built in previous work [Gilbert, 2025] and are used here to study the ability to complete dual-energy X-ray material discrimination at MeV energies. The work here is an interesting extension of the previous work because, rather than using X-ray and neutron data, the algorithm is constrained here to using only X-ray data, making the problem more ill-posed and difficult to solve.

The output from the inverse algorithm using the steel slabs object is shown in Figure 24. For this result, the steel slabs dual-energy data is given to the algorithm along with a two-material basis set of [Steel, W]. The result shows good discrimination between steel and tungsten in the regions where the steel is present. The material thicknesses are underestimated, and the thickness estimate does not appear uniform. This is a typical artifact of scattered radiation in a high energy radiograph, as shown in Figure 25, and will affect any quantitative analysis. In this particular case, the 3/4" of tungsten used to filter the spectrum was placed close to the image panel, which can make the scatter environment worse. Neither descattering nor deblurring methods were applied to this data before processing.

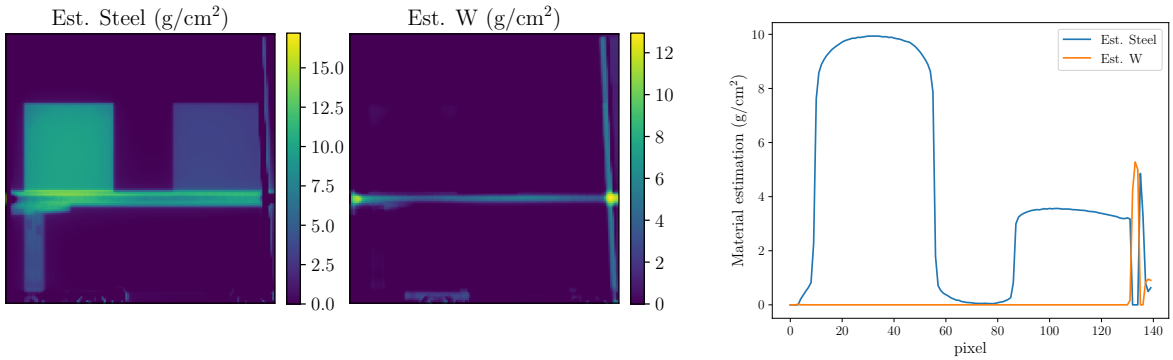


Figure 24. Steel slabs material estimations between steel and tungsten basis functions. Discrimination appears good, though accuracy is limited by the large scatter contribution shown in Figure 25. (left) Shows the materials estimated at each image pixel and (right) shows a line profile through the middle of the result images.

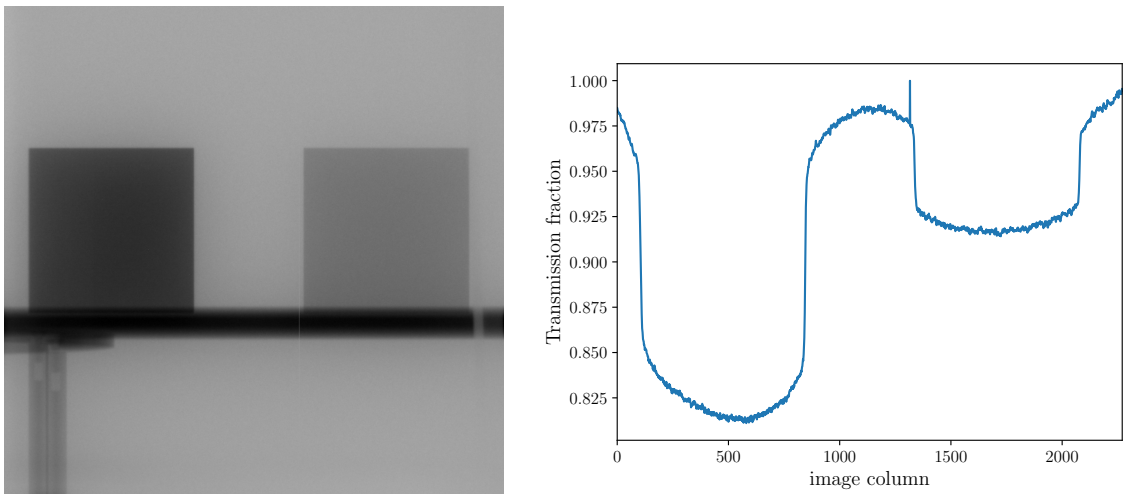


Figure 25. (left) Image data of the steel slabs object using high-energy spectrum with 3/4" thick tungsten for beam filtration. (right) The horizontal line profile of the data. Blurred material edges is a clear indication of a large scatter environment.

Material discrimination is not always of high quality. As explored in Section 2.0, there is limited information available in this type of data for material discrimination. While Figure 24 showed good discrimination between steel and tungsten, Figure 26 shows the result when the basis material set is steel and poly, which have much more similar attenuation profiles. The estimated thicknesses show approximately equal estimated thicknesses of the two materials, indicating material confusion and suggesting that the data does not support discriminating between materials in this range of atomic number Z. This is also supported in the Cramer Rao lower bound calculations shown in Section 2.0.

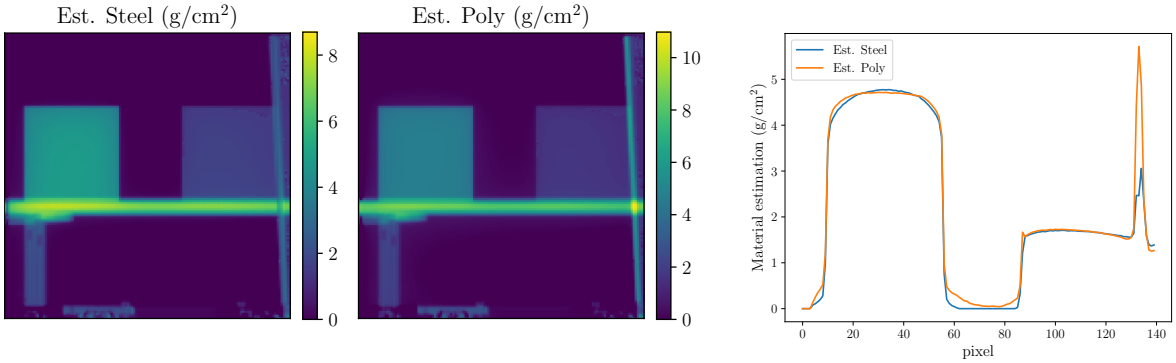


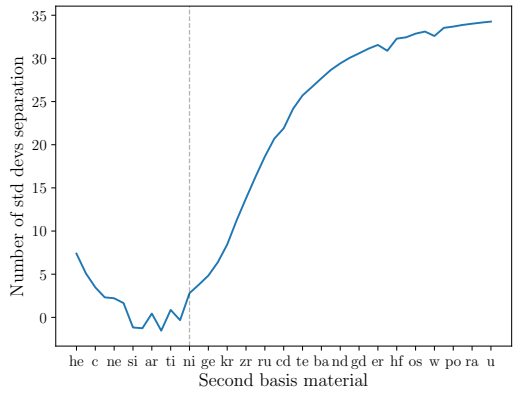
Figure 26. An example of material estimation algorithm results for a difficult material discrimination problem, here discriminating between basis functions of steel and poly.

In order to study the breadth of materials discrimination that would be available from dual-energy data like this, we frame the problem here similarly to that in Section 2.0. Using data from one of the slabs, we change the basis set of materials being estimated. One of the materials is set to the material that is present in the object while the other basis material is scanned over all elements in the periodic table. The measure of discrimination is the number of standard deviations between the mean estimated material thickness of the respective materials.

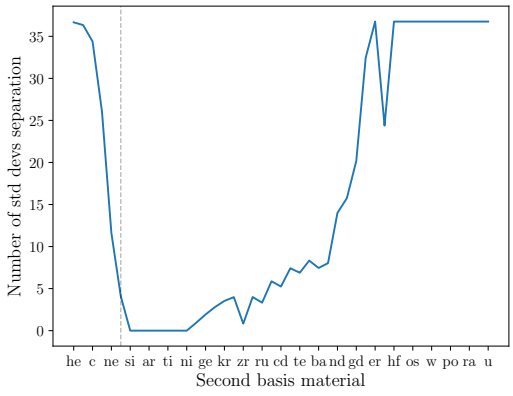
The result of this analysis is shown in Figure 27 for all the slab data. Each of these plots shows the separation between the material thicknesses estimates when the second material in the

material basis set is varied. Higher values indicate better discrimination. A vertical dotted line is drawn at the location where the basis materials are most similar in Z, a very difficult problem to solve with X-ray alone. A few observations can be made from these plots. First, discriminating between materials of similar Z is not possible. This is expected since the X-ray attenuation coefficients at these energies are very similar for materials with similar Z. Consistent with the studies in Section 2.0, it appears that discrimination between anything more than high-Z and low-Z is not possible at these energies. It is conceivable that the spectra and detector could be further optimized for better discrimination, but that will be left for a future study.

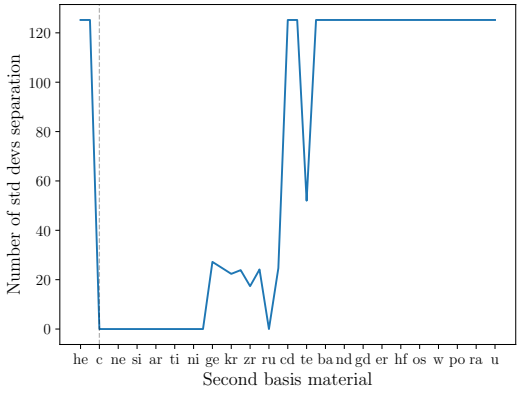
Second, the double peaks observed from the CRLB study, Figure 18, are not observed in these results. Importantly, the calculations in those results assumed a perfectly known physical model of the imaging system. In reality, there are a number of uncertainties in all portions of the physical model, from source spectrum to detector response to the transmitted beam. It is expected that these large systematic uncertainties will dominate the uncertainty in material discrimination. Third, the plot for discrimination for tungsten (W) appears altogether different than the others. This may be an indication that the physical model is poor for this data in particular, possibly due to differences in the scatter environment stemming from the different lateral dimensions of the objects (the tungsten slabs have a large area, 12” x 12”).



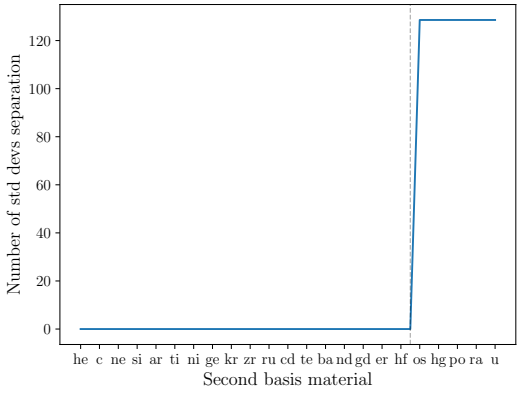
(a) Steel discrimination



(b) Al discrimination



(c) Poly discrimination



(d) W discrimination

Figure 27. A measure of materials discrimination (separation) is given for all of the slabs data. Higher values indicate that there is greater separation between the estimated slab material and that of the second basis material, scanned for all elements of the periodic table. Higher values are better and the dotted line indicates the location of the slab material on the x-axis.

Overall, the material discrimination results using experimental data and the inverse algorithm show trends consistent with those shown with the Cramer Rao calculations in Section 2.0. Systematic uncertainties in the physical model does affect the ability to make quantitative thickness estimations and will increase uncertainties compared to the Cramer Rao calculations. However, these results suggest that the Cramer Rao calculations can be used for experimental planning and to understand what can and cannot be determined from dual-energy X-ray data. This is important because high-energy, dual-energy X-ray radiography is not straightforward to acquire.

4.3 Material discrimination using a single-shot dual-energy grid

While the previous section explored what can be determined from a dual energy X-ray scan with an unfiltered and filtered spectrum of the same endpoint energy, putting a filter in the beam to take two X-ray shots may not be feasible in some end use cases. Therefore, we explore a method to make an effective dual-energy scan with a single image. Here, a “dual-energy” signal is acquired with a single X-ray shot through the use of a coarse grid which patterns the beam such that regions of filtered and unfiltered beam are observed in the image data. The grid designed for this project is shown in Figure 28 and the corresponding X-ray image is shown in Figure 29, where blocks of aluminum are visible along with the pattern created from the coarse grid. The grid has ¾” thick tungsten bars at a pitch (width of full grid period) of 1”.

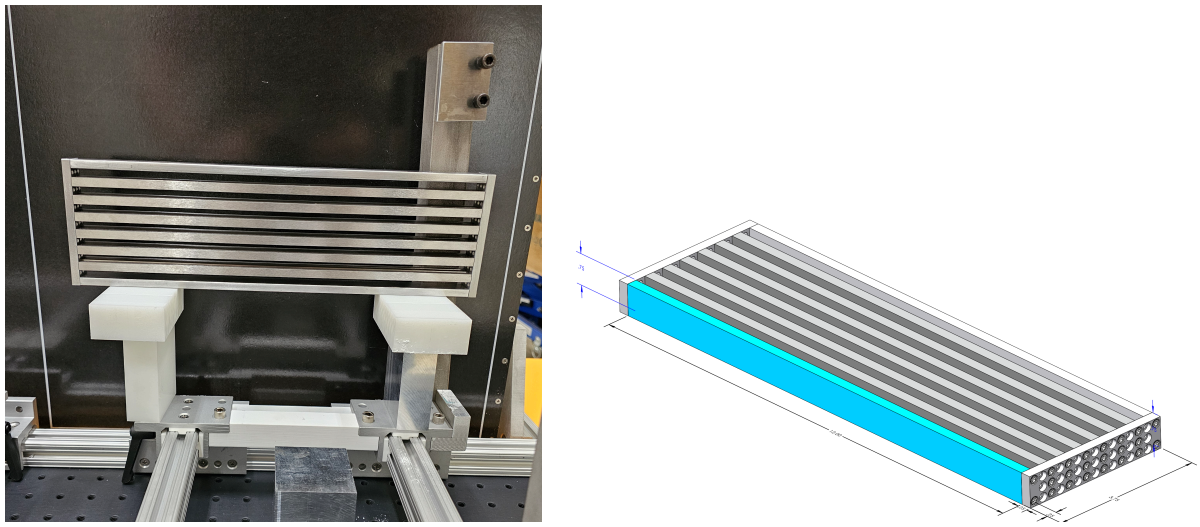


Figure 28. (left) A picture of the coarse grid placed in front of the image plane and (right) a drawing of the grid. This is a patterning element to be used to generate lower-energy (unfiltered) and higher-energy (filtered) data in a single image.

To create an effective dual-energy scan from the presence of a large grid in the image data, the image is first trimmed to include the grating with the width in pixels an integer multiple of the grating period. Each vertical line profile, such as is shown in Figure 30, was Fourier transformed. A Hann window was used to separate the zero-frequency component $\tilde{I}_0$ from the first harmonic contribution $\tilde{I}_1$. We assume the grid pattern is a square wave going from an intensity value of I_{lo} to I_{hi}, for which the Fourier series is

$$I(x) = \frac{(I_{lo} + I_{hi})}{2} + \frac{4}{\pi}(I_{hi} - I_{lo}) \sum_{n\ odd} \frac{1}{n} \sin\left[\frac{n\,\pi\,x}{L}\right].$$

We can reconstruct $(I_{hi} - I_{lo}) = \pi\, \tilde{I}_1/4$ and $(I_{lo} + I_{hi}) = 2\, \tilde{I}_0$, with the solution

$$I_{lo} = \tilde{I}_0 - \frac{\pi}{2}\, \tilde{I}_1$$

$$I_{hi} = \tilde{I}_0 + \frac{\pi}{2}\, \tilde{I}_1.$$

The result of this analysis is shown in the processed data shown in Figure 29, with the original image at top, the effective unfiltered spectrum objects at center, and the effective filtered spectrum objects at bottom.

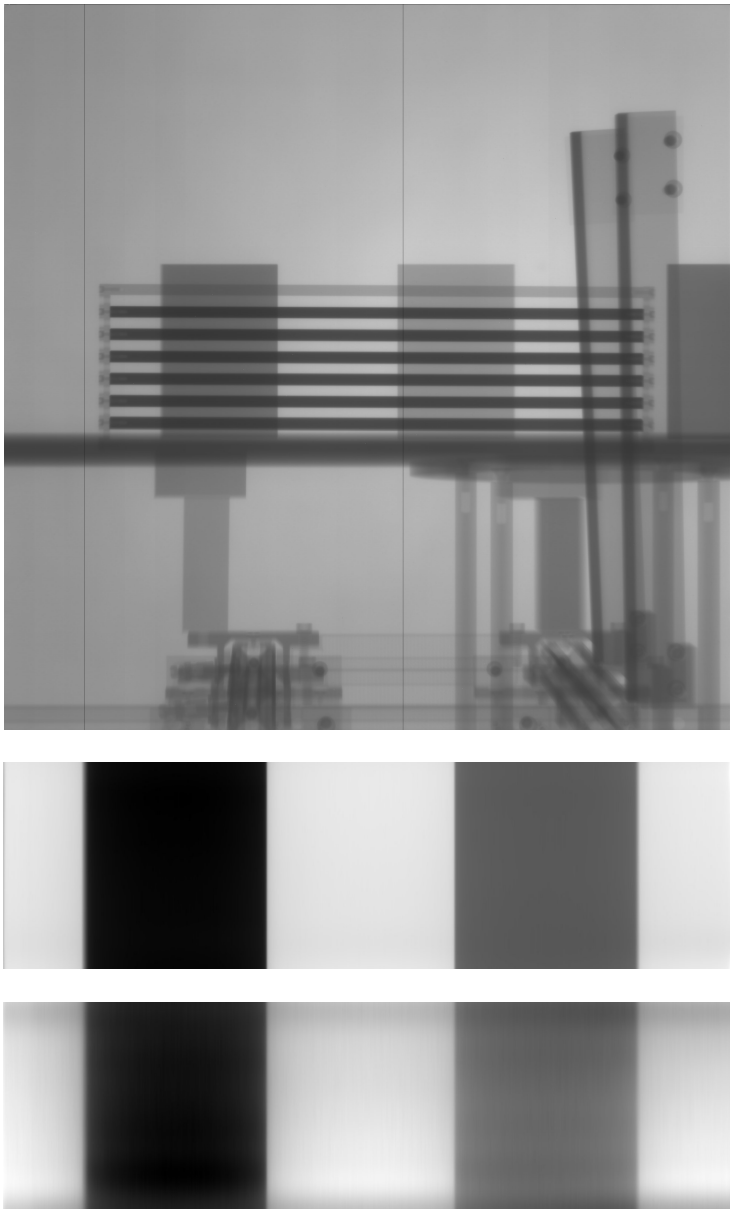


Figure 29. (top) The original image data with the coarse grid in place in the center of the image. This image also has two thicknesses of aluminum in front of the coarse grid. (middle) The processed unfiltered image data and (bottom) the processed filtered image data.

Since the spectra across the image plane are not well known for this data, the analysis used in the previous section will not be used here, which required an accurate model of the imaging system. A simpler way complete material identification is to compare the ratio of high-energy to low-energy attenuation by taking the negative log transform of the radiography data for each energy [Rinkel, 2011]. This ratio and how it changes with material thickness is a material signature.

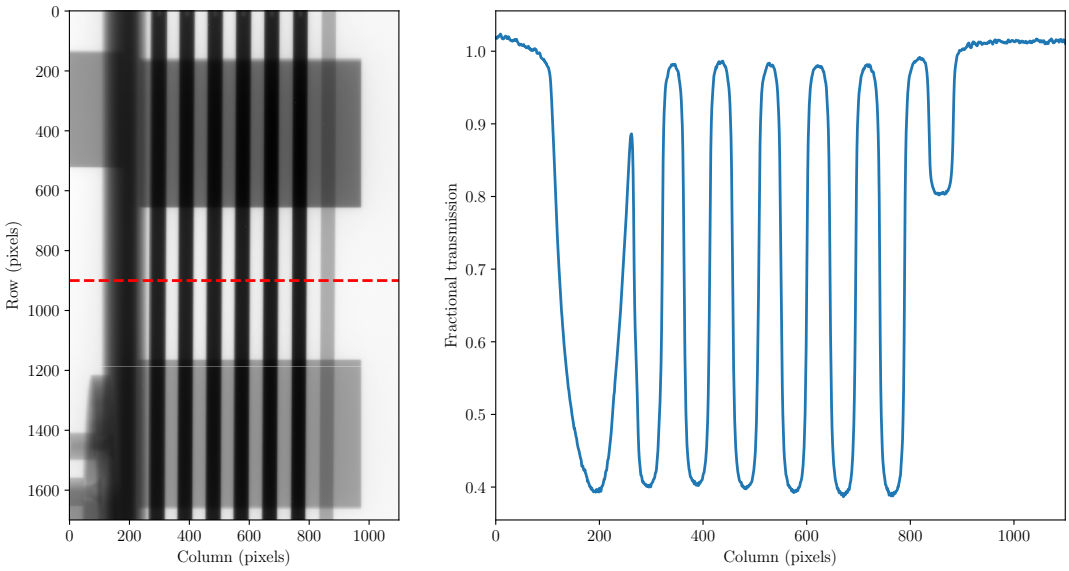


Figure 30. (left) A region of interest from the coarse grid data. (right) A line profile, shown in the left, from the grid data.

Figure 31 shows this analysis for the material slabs that have been introduced in previous sections, showing a line between the two thicknesses as a visual indication of the slope of the ratio with respect to material thickness. The reported mean values and associated errors are calculated from an ROI of the processed image data. The poly, aluminum, and iron show similar slope, an indication that discrimination between these materials would be very difficult. In contrast, the tungsten, while exhibiting a larger attenuation due to its high-density, does have a slope that appears significantly different from the other materials.

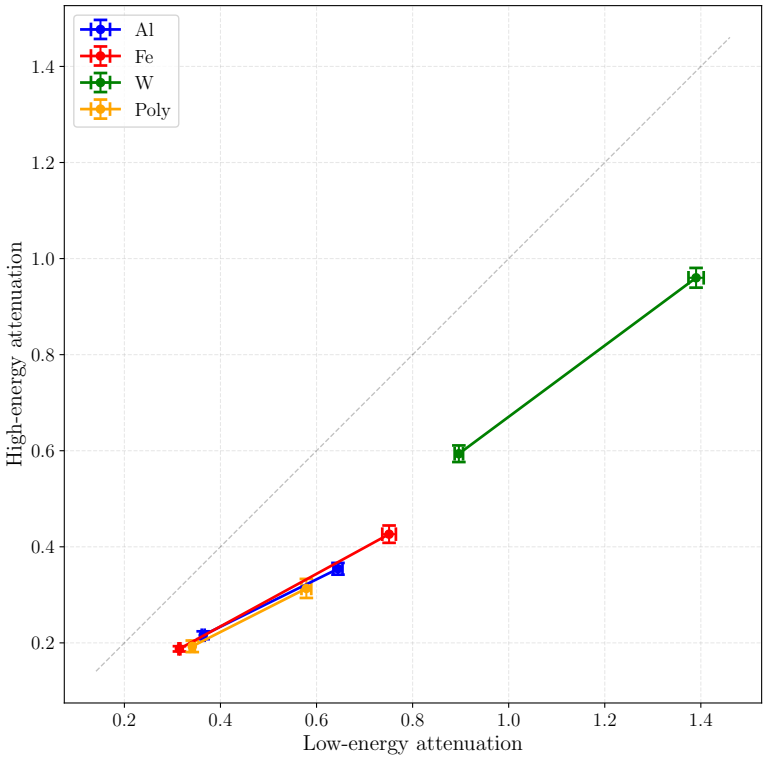


Figure 31. Low energy attenuation and high-energy attenuation calculated from regions of interest from the processed coarse grid data, e.g., Figure 29, for each material. The slope of the lines can be used for material identification.

Table 3. Summary of material slopes shown in Figure 31.

Material	Line slope
Poly	0.507 ± 0.100
Aluminum	0.493 ± 0.055
Steel	0.547 ± 0.047
Tungsten	0.742 ± 0.061

In summary, material discrimination appears possible with a single-shot dual-energy framework introduced in this section. The study is limited by a small number of materials and thicknesses, preventing any broader claims to be made. Nonetheless, the result is important in that it suggests that methods could be developed where time or space limitations limit the ability to complete a typical dual-energy scan. This approach does have additional complexities. First, as can be observed in Figure 30, the structure of the patterning element itself can affect results, with the transmitted values appearing to vary smoothly rather than abruptly with position; the absolute intensity in both the transmitting and the attenuating regions will not recover the values observed for a full field of view image. This does not appear to obscure the material difference present, however, and it may be possible to calibrate for this effect. Second, the Fourier

processing trades off spatial resolution to recover two images, with resolution reduced to the level of the period of the modulating period, in this case 1 inch. Using a finer optic would result in a higher resolution image, but may exacerbate the issues with spatial variations affecting intensities. Whether these tradeoffs are advantageous, and the optic design that best optimizes these tradeoffs, is a question that must be settled in the context of a specific application.

5.0 Conclusions and future work

This report has detailed a study of information contained in dual-energy radiography data for the purpose of materials discrimination, using computational methods and analysis of real high-energy, dual-energy X-ray radiography data.

In Section 2.0, we introduced and exercised a method, the Cramer Rao lower bound (CRLB), to compute the minimum uncertainty expected in determining a material thickness from the given radiography data. This study showed that material discrimination at MeV energies is difficult, largely driven by the fact that the X-ray attenuation coefficients for a wide range of material Z show similar energy-dependent profiles largely due to Compton scatter effects that dominate the X-ray interactions from ~500 keV to ~ 4 MeV. Due to the physics of X-ray attenuation, there is limited material information available from X-ray radiography data in these energies independent of the algorithms used for material extraction. Nonetheless, discrimination between high-Z and low-Z materials appears feasible. Further studies showed that filtering the beam with high-Z filters aids material discrimination compared to filtering with low-Z filters. Furthermore, using a lower-energy endpoint for the unfiltered spectrum, such as 4 MeV, for data acquisition may not be better if the strength of the source is lowered at those endpoints, such as is typical for X-ray betatron sources.

In Section 3.0, we used physical models and introduced an inverse algorithm to determine material thicknesses from the dual-energy radiography data. This allowed comparison of uncertainties observed from the output of an inverse algorithm, a least-squares misfit, and how it compares to the uncertainties calculated from the CRLB. We found good agreement between trends of the algorithm output compared to the CRLB calculations, comparing results when the X-ray spectra used for the inspection are varied. Furthermore, we explored the effect of systematic uncertainties in the physics model used in the inverse algorithm. The CRLB cannot capture the effect systematic uncertainties, only random uncertainties. It was found that inaccurate scatter models affect material discrimination considerably. However, if the scatter is known to good accuracy (either via modeling or calibration during measurement) and used in the inverse algorithm, the systematic errors are corrected and nominal material discrimination is recovered.

In Section 4.0, the theoretical work in the previous sections was tested with real high-energy, dual-energy X-ray radiography. We find that the CRLB calculations compare well to material discrimination observed with real data and the inverse algorithm. The ability to complete accurate material estimation requires accurate physical models, and the work was somewhat limited here by the presence of scatter, and our ability to characterize it, in the radiography data. Furthermore, this section detailed the feasibility of completing dual-energy radiography in a single image shot through the use of a coarse grid that produces interspersed attenuated and unattenuated regions in the image. Though this does reduce the effective spatial resolution of the system, preliminary results indicate that material discrimination between low- and high-Z materials is feasible in this regime. This is an important conclusion that indicates methods like this could be used for material discrimination when time or space limitations prevent a full dual-energy scan to be made.

The ability to complete material discrimination with high-energy X-ray radiography is limited, largely by the limited material information that is encoded in the transmitted X-ray beam. Options for future research are listed here.

1. Targeted imaging system design with the Cramer-Rao lower bound (CRLB). The work presented here shows that uncertainties from the CRLB track well with uncertainties from an inverse algorithm and real X-ray data. This suggests that the CRLB calculations could be used to determine what level of information can be determined from the radiography data, and how to design the system better to increase the information available from the data. For example, calculations like this would help to frame developments in X-ray sources and detectors that would be particularly beneficial for a given task. As monoenergetic sources are designed, higher-efficiency detector materials are developed, and high-energy spectral imaging becomes feasible, bringing methods like this alongside the equipment development could be beneficial to inform which capabilities of future high-energy radiography systems will be particularly beneficial for material discrimination.

2. Development of fast, accurate physics (forward) models for high-energy radiography systems. Computational studies in this report show the importance of having an accurate physics model for any quantitative image analysis. High-energy radiography systems used in this report could be better understood. In particular, the report found that knowing the X-ray spectrum and reducing or estimating the scatter component is particularly important. Low-energy X-ray radiography systems in the 100s-of-keV range are well understood given their ubiquitous use in the medical and security fields. While high-energy radiography systems can be niche in their uses, their range of use is increasing, particularly for cargo inspection and nondestructive evaluation.

3. Imaging system design for completing single-shot, dual-energy radiography using a coarse grating. Experiments presented here were preliminary and explored a limited range of material geometries and compositions. However, the results suggest that more can be done here to enable single-shot dual-energy radiography. Further exploration of grid design, including the trade-offs between grid period and available information, would make the method fieldable. This single-shot method would be useful the time or space constraints limit the ability to complete a pair of X-ray shots for dual-energy imaging.

6.0 References

S. G. Azevedo, H. E. Martz, M. B. Aufderheide, W. D. Brown, K. M. Champley, J. S. Kallman, G. P. Roberson, D. Schneberk, I. M. Seetho, and J. A. Smith, “System-independent characterization of materials using dual-energy computed tomography,” *IEEE Transactions on Nuclear Science*, vol. 63, no. 1, pp. 341–350, 2016. https://doi.org/10.1109/TNS.2016.2514364

L. W. Campbell, A. J. Gilbert, and R. S. Wittman, “Scatter and blur corrections for high-energy x-ray radiography,” *IEEE Transactions on Nuclear Science*, 2025. https://doi.org/10.1109/TNS.2025.3539686

A. Fainberg, “Explosives detection for aviation security,” *Science*, vol. 255, no. 5051, pp. 1531–1537, 1992. https://doi.org/10.1126/science.255.5051.1531

A. J. Gilbert, B. S. McDonald, and M. R. Deinert, “Advanced algorithms for radiographic material discrimination and inspection system design,” *Nuclear Instruments and Methods in Physics Research Section B*, vol. 385, pp. 51–58, 2016. https://dx.doi.org/10.1016/j.nimb.2016.07.013

A. J. Gilbert, B. S. McDonald, and M. R. Deinert, “Inverse method for noninvasive material discrimination with multienergy x-ray radiography,” *Phys. Rev. Applied*, vol. 18, p. 054043, Nov 2022. https://doi.org/10.1103/PhysRevApplied.18.054043

A. J. Gilbert, L. W. Campbell, N. Deshmukh, P. A. Hausladen, M. R. Heath, D. M. Kasparek, L. A. Misurek, P. B. Rose, and K. T. Schmitt, “X-ray and neutron radiography for quantitative material reconstructions,” *IEEE Transactions on Nuclear Science*, vol. 72, no. 7, pp. 2183–2193, 2025. https://doi.org/10.1109/TNS.2025.3572420

E. A. Miller, D. M. Kasparek, L. W. Campbell, T. A. White, P. Rose, “Advanced Methods for High Energy Radiography: Collimation Feasibility Report,” *PNNL-37001*, 2024.

S. Ogorodnikov and V. Petrunin, “Processing of interlaced images in 4-10 MeV dual energy customs system for material recognition,” *Physical Review Special Topics - Accelerators and Beams*, vol. 5, no. 10, pp. 104701, 1–11, 2002. https://dx.doi.org/10.1103/PhysRevSTAB.5.104701

J. Rinkel, G. Beldjoudi, V. Rebuffel, C. Boudou, P. Ouvrier-Buffet, G. Gonon, L. Verger, and A. Brambilla, “Experimental evaluation of material identification methods with CdTe X-ray spectrometric detector,” IEEE Transactions on Nuclear Science, vol. 58, no. 5, pp. 2371–2377, 2011. https://doi.org/10.1109/tns.2011.2164266

E. Roessl and C. Herrmann, “Cramér-Rao lower bound of basis image noise in multiple-energy x-ray imaging”, Physics in Medicine and Biology **54** (2009) 1307-1318, http://dx.doi.org/10.1088/0031-9155/54/5/014

R. Runkle, T. White, E. Miller, J. Caggiano, and B. Collins, “Photon and neutron interrogation techniques for chemical explosives detection in air cargo: A critical review,” Nuclear Instruments and Methods in Physics Research Section A, vol. 603, no. 3, pp. 510–528, 2009. https://doi.org/10.1016/j.nima.2009.02.015

B. Tobias and M. L. Klasky, “Limits of special material detectability fundamental to idealized dual-energy radiographic systems,” *Nuclear Instruments and Methods in Physics Research Section A*, vol. 944, p. 162563, 2019. https://doi.org/10.1016/j.nima.2019.162563

Appendix A – Cramer Rao lower bound calculation raw results

The results of the uncertainties from the information matrix are presented here. Each section separated by a line of dashes is using the estimated signal behind a block of material described in the first line. Each paragraph after that examines the hypothesis that the block is composed of two materials (one of which may or may not be the actual material from which the block is known to be made). The first line of the paragraph gives the names of the two materials. The next two lines give the lower bound uncertainty of any estimate for the areal density of the material. The subsequent line is the condition number of the information matrix. Finally, the lower bound covariance matrix is printed.

```
------------------------------------------------------
HDPE_2.125_in_(5.4_g/cm²)

Poly, Al
    Poly      ±165.786 g/cm²
      Al      ±191.94 g/cm²
  condition number: 1.63949e+06
  covariance
   27485.1   -31820.9
    -31821    36840.9

Poly, Fe
    Poly      ±14.486 g/cm²
      Fe      ±15.4944 g/cm²
  condition number: 12306
  covariance
   209.844   -224.415
  -224.415    240.076

Poly, W
    Poly      ±1.36274 g/cm²
       W      ±0.466635 g/cm²
  condition number: 286.578
  covariance
   1.85706  -0.624064
 -0.624064   0.217749

Al, Fe
      Al      ±15.4238 g/cm²
      Fe      ±14.2495 g/cm²
  condition number: 10425.8
  covariance
   237.893   -219.739
  -219.739    203.049

Al, W
      Al      ±1.5651 g/cm²
       W      ±0.462902 g/cm²
```

```
  condition number: 358.626
  covariance
   2.44953  -0.710777
 -0.710777   0.214278

Fe, W
      Fe      ±1.60615 g/cm²
       W      ±0.51419 g/cm²
  condition number: 388.35
  covariance
   2.57971  -0.813223
 -0.813223   0.264392

------------------------------------------------------
HDPE_4.25_in_(11_g/cm²)

Poly, Al
    Poly      ±112.927 g/cm²
      Al      ±130.791 g/cm²
  condition number: 561959
  covariance
   12752.4   -14769.6
  -14769.9    17106.4

Poly, Fe
    Poly      ±24.9587 g/cm²
      Fe      ±27.1446 g/cm²
  condition number: 27054.8
  covariance
   622.937   -677.442
  -677.442    736.827

Poly, W
    Poly      ±1.63806 g/cm²
       W      ±0.652515 g/cm²
  condition number: 242.778
  covariance
   2.68324   -1.05022
  -1.05022   0.425775

Al, Fe
      Al      ±23.6748 g/cm²
      Fe      ±22.2315 g/cm²
  condition number: 18091
  covariance
   560.497   -526.269
  -526.269     494.24

Al, W
      Al      ±1.87052 g/cm²
       W      ±0.643348 g/cm²
  condition number: 295.323
```

```
  covariance
   3.49886   -1.18181
  -1.18181   0.413896

Fe, W
      Fe      ±1.90447 g/cm²
       W      ±0.697549 g/cm²
  condition number: 315.017
  covariance
   3.62702   -1.30822
  -1.30822   0.486575

-----------------------------------------------------
Al_1_in_(6.9_g/cm²)

Poly, Al
    Poly      ±153.216 g/cm²
      Al      ±177.475 g/cm²
  condition number: 1.35954e+06
  covariance
   23475.2   -27192.1
  -27191.8    31497.3

Poly, Fe
    Poly      ±15.7528 g/cm²
      Fe      ±16.931 g/cm²
  condition number: 14136.7
  covariance
   248.151   -266.673
  -266.673     286.66

Poly, W
    Poly      ±1.39634 g/cm²
       W      ±0.494275 g/cm²
  condition number: 277.214
  covariance
   1.94976   -0.67757
  -0.67757   0.244307

Al, Fe
      Al      ±16.5461 g/cm²
      Fe      ±15.3528 g/cm²
  condition number: 11628.3
  covariance
   273.773   -253.984
  -253.984    235.707

Al, W
      Al      ±1.60309 g/cm²
       W      ±0.489892 g/cm²
  condition number: 345.442
  covariance
```

```
   2.56989  -0.770737
 -0.770737   0.239994

Fe, W
      Fe      ±1.64408 g/cm²
       W      ±0.541471 g/cm²
  condition number: 373.591
  covariance
   2.70301  -0.876697
 -0.876697   0.293191

-----------------------------------------------------
Al_2_in_(13.7_g/cm²)

Poly, Al
    Poly      ±106.606 g/cm²
      Al      ±123.554 g/cm²
  condition number: 471569
  covariance
   11364.9   -13171.5
  -13171.6    15265.6

Poly, Fe
    Poly      ±30.7939 g/cm²
      Fe      ±33.7401 g/cm²
  condition number: 38823
  covariance
   948.267   -1038.94
  -1038.94     1138.4

Poly, W
    Poly      ±1.72683 g/cm²
       W      ±0.731541 g/cm²
  condition number: 232.629
  covariance
   2.98194    -1.2422
   -1.2422   0.535153

Al, Fe
      Al      ±27.691 g/cm²
      Fe      ±26.1788 g/cm²
  condition number: 23250.3
  covariance
   766.794   -724.855
  -724.855    685.328

Al, W
      Al      ±1.96997 g/cm²
       W      ±0.720075 g/cm²
  condition number: 280.073
  covariance
   3.88078   -1.39413
```

```
  -1.39413   0.518508

Fe, W
      Fe      ±2.00257 g/cm²
       W      ±0.774278 g/cm²
  condition number: 297.712
  covariance
    4.0103   -1.52751
  -1.52751   0.599506

-----------------------------------------------------
Steel_1/4_in_(5.0_g/cm²)

Poly, Al
    Poly      ±135.249 g/cm²
      Al      ±156.914 g/cm²
  condition number: 1.10468e+06
  covariance
   18292.2   -21221.4
  -21223.3      24622

Poly, Fe
    Poly      ±17.718 g/cm²
      Fe      ±19.2452 g/cm²
  condition number: 18670.3
  covariance
   313.928    -340.95
   -340.95    370.377

Poly, W
    Poly      ±1.40031 g/cm²
       W      ±0.528504 g/cm²
  condition number: 263.343
  covariance
   1.96087   -0.72718
  -0.72718   0.279317

Al, Fe
      Al      ±18.1748 g/cm²
      Fe      ±17.0164 g/cm²
  condition number: 14559.5
  covariance
   330.322   -309.226
  -309.226    289.557

Al, W
      Al      ±1.60819 g/cm²
       W      ±0.523183 g/cm²
  condition number: 325.905
  covariance
   2.58628  -0.826422
 -0.826422    0.27372
```

```
Fe, W
      Fe      ±1.64926 g/cm²
       W      ±0.573069 g/cm²
  condition number: 352.222
  covariance
   2.72006  -0.931157
 -0.931157   0.328408

-----------------------------------------------------
Steel_3/4_in_(15.0_g/cm²)

Poly, Al
    Poly      ±86.6431 g/cm²
      Al      ±100.67 g/cm²
  condition number: 271044
  covariance
   7507.02   -8722.23
  -8722.28    10134.4

Poly, Fe
    Poly      ±150.584 g/cm²
      Fe      ±169.388 g/cm²
  condition number: 811713
  covariance
   22675.5   -25506.2
  -25507.9    28692.4

Poly, W
    Poly      ±2.18562 g/cm²
       W      ±1.1868 g/cm²
  condition number: 237.745
  covariance
   4.77692   -2.56295
  -2.56295     1.4085

Al, Fe
      Al      ±63.9028 g/cm²
      Fe      ±61.8652 g/cm²
  condition number: 106904
  covariance
   4083.57   -3953.29
  -3953.29    3827.31

Al, W
      Al      ±2.4777 g/cm²
       W      ±1.15795 g/cm²
  condition number: 270.802
  covariance
     6.139   -2.83308
  -2.83308    1.34085
```

```
Fe, W
      Fe      ±2.49424 g/cm²
       W      ±1.20407 g/cm²
  condition number: 281.133
  covariance
   6.22124   -2.96844
  -2.96844    1.44979

-----------------------------------------------------
W_1/4_in_(12.2_g/cm²)

Poly, Al
    Poly      ±88.1561 g/cm²
      Al      ±102.508 g/cm²
  condition number: 190883
  covariance
    7771.5    -9036.6
   -9036.6    10507.9

Poly, Fe
    Poly      ±45.7942 g/cm²
      Fe      ±53.0686 g/cm²
  condition number: 51455.9
  covariance
   2097.11   -2430.14
  -2430.14    2816.28

Poly, W
    Poly      ±9.414 g/cm²
       W      ±8.48363 g/cm²
  condition number: 2149.13
  covariance
   88.6234   -79.7898
  -79.7898    71.9719

Al, Fe
      Al      ±110.811 g/cm²
      Fe      ±110.435 g/cm²
  condition number: 218064
  covariance
   12279.1   -12237.3
  -12237.3    12195.9

Al, W
      Al      ±9.89141 g/cm²
       W      ±7.66586 g/cm²
  condition number: 1850.88
  covariance
   97.8401   -75.7389
  -75.7389    58.7654

Fe, W
```

```
      Fe      ±9.05091 g/cm²
       W      ±7.03838 g/cm²
  condition number: 1557.33
  covariance
    81.919   -63.6167
  -63.6167    49.5387

-------------------------------------------------------
W_3/4_in_(36.7_g/cm²)

Poly, Al
    Poly      ±83.5471 g/cm²
      Al      ±95.4136 g/cm²
  condition number: 142706
  covariance
   6980.11   -7971.64
  -7971.64    9103.76

Poly, Fe
    Poly      ±36.8494 g/cm²
      Fe      ±41.1329 g/cm²
  condition number: 27610.3
  covariance
   1357.88   -1515.84
  -1515.84    1691.91

Poly, W
    Poly      ±123.854 g/cm²
       W      ±122.355 g/cm²
  condition number: 308196
  covariance
   15339.8   -15154.2
  -15154.3    14970.8

Al, Fe
      Al      ±75.294 g/cm²
      Fe      ±73.5935 g/cm²
  condition number: 87364.8
  covariance
   5669.19   -5541.28
  -5541.28    5416.01

Al, W
      Al      ±293.179 g/cm²
       W      ±253.611 g/cm²
  condition number: 1.35191e+06
  covariance
   85954.2   -74353.1
    -74354    64318.4

Fe, W
      Fe      ±58.5553 g/cm²
```

```
      W      ±51.8224 g/cm²
  condition number: 56108.9
  covariance
   3428.72   -3034.59
  -3034.59    2685.57

-----------------------------------------------------
```

Pacific Northwest National Laboratory

902 Battelle Boulevard
P.O. Box 999
Richland, WA 99354
1-888-375-PNNL (7665)

www.pnnl.gov